

# Microphysical Model of Jupiter’s Great Red Spot Upper Chromophore Haze

Asier Anguiano-Arteaga<sup>a,b,\*</sup>, Santiago Pérez-Hoyos<sup>a</sup>, Agustín Sánchez-Lavega<sup>a</sup>, Patrick G.J. Irwin<sup>b</sup>

<sup>a</sup>*Dpto. Física Aplicada, EIB, Universidad del País Vasco UPV/EHU, Bilbao, Spain*

<sup>b</sup>*Department of Physics, Atmospheric, Oceanic and Planetary Physics, University of Oxford, Oxford, United Kingdom*

---

## Abstract

The origin of the red colouration in Jupiter’s Great Red Spot (GRS) is a long-standing question in planetary science. While several candidate chromophores have been proposed, no clear conclusions have been reached regarding its nature, evolution, or relationship to atmospheric dynamics. In this work, we perform microphysical simulations of the reddish haze over the GRS and quantify the production rates and timescales required to sustain it. Matching the previously reported chromophore column mass and effective radius in the GRS requires column-integrated injection fluxes in the range  $1 \times 10^{-12} - 7 \times 10^{-12} \text{ kg m}^{-2} \text{ s}^{-1}$ , under low upwelling velocities in the upper troposphere ( $v_{\text{trop}} \lesssim 1.5 \times 10^{-4} \text{ m s}^{-1}$ ) and particle charges of at least 20 electrons/ $\mu\text{m}$ . Such rates exceed the mass flux that standard photochemical models of Jupiter currently supply via  $\text{NH}_3\text{--C}_2\text{H}_2$  photochemistry at 0.1–0.2 bar, the most popular chromophore pathway in recent literature. We find a lower limit of 7 years on the haze formation time. We also assess commonly used size and vertical distribution parameterisations for the chromophore haze, finding that eddy diffusion prevents the long-term confinement of a thin layer and that the extinction is dominated by particles that can be represented by a single log-normal size distribution.

*Keywords:* Jupiter, Atmosphere, Great Red Spot, Microphysics

---

<sup>\*</sup>Corresponding author.

*Email address:* `asier.anguiano@ehu.eus` (Asier Anguiano-Arteaga)

## 1. Introduction

Jupiter's Great Red Spot (GRS) is one of the most striking features in any planetary atmosphere. It is the largest anticyclone ever observed and also the longest-lived. Once thought to have been first observed by Giovanni Cassini in 1665, recent evidence indicates that the GRS was most likely first reported in 1831 and originated from a flow disturbance between the westward zonal jet at 20°S and the eastward jet at 26°S (Sánchez-Lavega et al., 2024). Since the Voyager 1 and 2 Jupiter flybys (Conrath et al., 1981; Flasar et al., 1981; Mitchell et al., 1981), the GRS has been extensively studied. However, many aspects of its structure, internal dynamics, and composition remain uncertain.

Although Jupiter's colours are often exaggerated by image processing (Ordóñez-Etxeberria et al., 2016; Irwin et al., 2024), the Great Red Spot's remarkable reddish coloration is still one of its most debated aspects. The jovian condensable species predicted from thermochemical equilibrium models are white at visible wavelengths (West et al., 1986, 2004). These species cannot account for the broad blue-light absorption that is observed not only in the GRS, but over all the planet, including whitish regions such as the South Tropical Zone (Anguiano-Arteaga et al., 2021). The source of the jovian coloration is generally attributed to the optical properties and distribution of aerosols above the 1-bar pressure level (Banfield et al., 1998). A number of colouring aerosols, commonly referred to as chromophores, have been proposed, and a comprehensive review is given by West et al. (1986, 2004). More recently, Loeffler et al. (2016) proposed irradiated ammonia hydrosulfide as a possible chromophore for the GRS, although its laboratory spectra show a distinct absorption band near 600 nm and comparatively weak absorption at wavelengths longer than 500 nm, features not seen in the GRS or other Jovian spectra (Dahl et al., 2021).

The most popular chromophore candidate to date is the suite of products resulting from photolyzed ammonia reacting with acetylene (Carlson et al., 2016). These compounds, previously explored by Ferris & Ishikawa (1987), are an attractive candidate because acetylene is the third most abundant hydrocarbon species in Jupiter after methane and ethane, and ammonia is the fifth most abundant compound after hydrogen, helium, methane, and water (Sánchez-Lavega, 2011). Carlson et al. (2016) did not identify a single specific compound responsible for the chromophore, but instead characterized a family of laboratory-produced residues with molecular formulae  $C_{2n}H_{4n-2}N_2$ ,

$C_{2n}H_{4n}N_2$  and  $C_{2n}H_{4n+2}N_2$ , with the  $H_{4n}$  series being the most abundant. The associated wavelength-dependent imaginary refractive indices provided by [Carlson et al. \(2016\)](#), corresponding to a 70 h irradiated sample, have been shown to reproduce different Jovian spectra ([Sromovsky et al., 2017](#); [Braude et al., 2020](#); [Pérez-Hoyos et al., 2020](#); [Dahl et al., 2021](#); [Anguiano-Arteaga et al., 2021, 2023](#); [Fry and Sromovsky, 2023](#)), including spectra specifically of the GRS ([Baines et al., 2019](#); [Braude et al., 2020](#); [Anguiano-Arteaga et al., 2021, 2023](#)), with little or no modification. A widely adopted chromophore configuration is the so-called Crème-Brûlée model, in which the chromophore is confined to a thin layer above the main tropospheric cloud. This configuration was first proposed for the Great Red Spot (GRS) by [Baines et al. \(2016\)](#), and later extended to other regions across the planet. Notably, [Sromovsky et al. \(2017\)](#) suggested that the Carlson chromophore could act as a universal colouring agent throughout Jupiter’s atmosphere.

Although the spectral behaviour of Carlson’s chromophore is plausible, the photochemical modelling of [Moses et al. \(2010\)](#) points to weak coupling between acetylene and ammonia in Jupiter’s troposphere as a result of the low diffusive flux at the tropopause. This issue was explored by [Baines et al. \(2019\)](#), who estimated the diffusive flux of  $C_2H_2$  into the high troposphere and concluded that an enhanced  $C_2H_2$  supply would be required to generate the observed chromophore within plausible timescales (from  $\sim 1.5$  months to  $\sim 11.5$  years). As a possible source of this enhancement, [Baines et al. \(2019\)](#) invoked lightning–driven production of  $C_2H_2$ , as previously proposed for Jupiter by [Bar-Nun & Podolak \(1985\)](#) and [Podolak & Bar-Nun \(1988\)](#). However, the [Baines et al. \(2019\)](#) estimates assume a vertically constant eddy diffusion coefficient and neglect sedimentation, which becomes increasingly important as particles grow and would remove material from the production region.

Building on this, a dedicated microphysical treatment is needed. Radiative transfer studies constrain the chromophore’s effective radius, column mass, and pressure level in the GRS, but they do not by themselves tell us what particle injection rates, vertical transport, and coagulation are required to maintain such a layer. A one–dimensional microphysical model that explicitly includes sedimentation, eddy diffusion, and particle growth provides this link: it allows us to derive the mass–injection rates needed to sustain the retrieved chromophore layer under physically plausible vertical velocities and particle sizes.

In this work, we develop a one–dimensional microphysical model for the

GRS chromophore haze and use it to quantify the required production rates and timescales. Section 2 describes the model formulation, the adopted GRS atmospheric structure and eddy–diffusion profile, and the radiative transfer constraints on chromophore mass column density, particle size, and pressure level that we aim to reproduce for the [Carlson et al. \(2016\)](#) chromophore. We then define the parameter space explored. In Section 3, we present the subset of simulations that match the retrieved chromophore properties in the GRS, derive the corresponding mass–injection rates and convergence timescales. In Section 4, we interpret these results in terms of the availability of precursor gases ( $\text{C}_2\text{H}_2$  and  $\text{NH}_3$ ) and the resulting particle size and vertical distributions. Our main conclusions are summarised in Section 5. Finally, [Appendix A](#) validates the numerical implementation of the transport and coagulation schemes against analytical solutions.

## 2. Microphysical model

### 2.1. Haze microphysics

We have developed a one-dimensional microphysical code based on the algorithms of [Toon et al. \(1988\)](#). The code assumes that spherical particles of a specified size are produced at a given atmospheric altitude as a result of chemical reactions. These particles are subject to sedimentation, eddy diffusion, and coagulation. Sedimentation and eddy diffusion govern vertical transport, while coagulation alters the particle size distribution. Condensation and evaporation are not considered, as [Carlson et al. \(2016\)](#) indicate that their proposed chromophore is a non-volatile solid residue. Using radiative transfer retrievals, [Sromovsky et al. \(2017\)](#) and [Baines et al. \(2019\)](#) investigated whether this chromophore could appear as a coating on main tropospheric cloud particles, but found that this assumption led to significantly poorer fits to Cassini VIMS spectra of both the Great Red Spot (GRS) and other Jovian regions. Our method, in which the haze grows only by coagulation, is therefore similar to the approaches of [Toon et al. \(1980\)](#) for Titan, [Toledo et al. \(2019\)](#) for Uranus and [Toledo et al. \(2020\)](#) for Neptune.

The aerosol continuity equation on which our model is based can be written as follows:

$$\begin{aligned}
\frac{\partial C(z, r)}{\partial t} = & C_{\text{inj}}(z, r) \\
& + \frac{\partial [K_{zz}(z)\rho]}{\partial z} \frac{\partial}{\partial z} \left[ \frac{C(z, r)}{\rho} \right] - \frac{\partial [W(z, r)C(z, r)]}{\partial z} \\
& + P_{\text{coag}}(z, r) - L_{\text{coag}}(z, r)
\end{aligned} \tag{1}$$

Here,  $C(z, r)$  represents the number density of haze particles of radius  $r$  at altitude  $z$ , and  $C_{\text{inj}}(z, r)$  denotes the injection rate of such particles at that level. The second and third terms on the right-hand side describe vertical transport: the former accounts for eddy diffusion, involving the eddy diffusion coefficient  $K_{zz}(z)$  and the atmospheric gas density  $\rho$ , and the latter captures the effects of gravitational sedimentation and vertical advection via the vertical velocity  $W(z, r)$ . Finally, the last two terms account for the net effect of coagulation on particles of radius  $r$ : their production by aggregation of smaller particles, and their loss due to coagulation with particles of the same or different sizes, respectively.

This formalism builds upon the one-dimensional model originally developed by [Turco et al. \(1979a\)](#) and [Toon et al. \(1979\)](#). Various versions of this model have been widely used to study the atmospheres of Solar System bodies ([Pollack et al., 1987](#); [Cabane et al., 1992](#); [Moreno, 1996](#); [Colaprete and Toon, 2003](#); [McGouldrick and Toon, 2007](#); [Toledo et al., 2020](#)), as well as those of exoplanets ([Marley et al., 2013](#); [Gao et al., 2017](#)). Numerical validations of our code are presented in [Appendix A](#).

## 2.2. Atmospheric profiles in the GRS

For the pressure–temperature (P–T) profile, we used the one derived from TEXES/Gemini North observations in March 2017, as published in the supplementary material of [Fletcher et al. \(2020\)](#). Although that work focuses on the North Equatorial Belt, the same retrieval methodology was applied across a broad pressure range (10 to  $10^{-6}$  bar) and spatial domain (planeto-centric latitudes  $0^\circ$  to  $26.5^\circ\text{S}$ , SIII west longitudes  $5^\circ$  to  $55^\circ$ ), encompassing the location of the GRS at the time of the observations. To construct the P–T profile, we averaged temperatures over a  $3 \times 3$  pixel region within the GRS, based on a map with a spatial resolution of  $1^\circ$  per pixel in both latitude and longitude. From the resulting P–T profile, air density was computed using the ideal gas law, and pressure was converted to altitude via the hydrostatic equilibrium equation, assuming an effective gravitational acceleration

of  $g = 23.17 \text{ m s}^{-2}$  at the GRS planetocentric latitude of  $20.5^\circ\text{S}$ . The resulting profile is shown in Fig. 1. As a consistency check, we compared these profiles with those presented by Gladstone et al. (1996), and found, despite expected differences, good overall agreement.

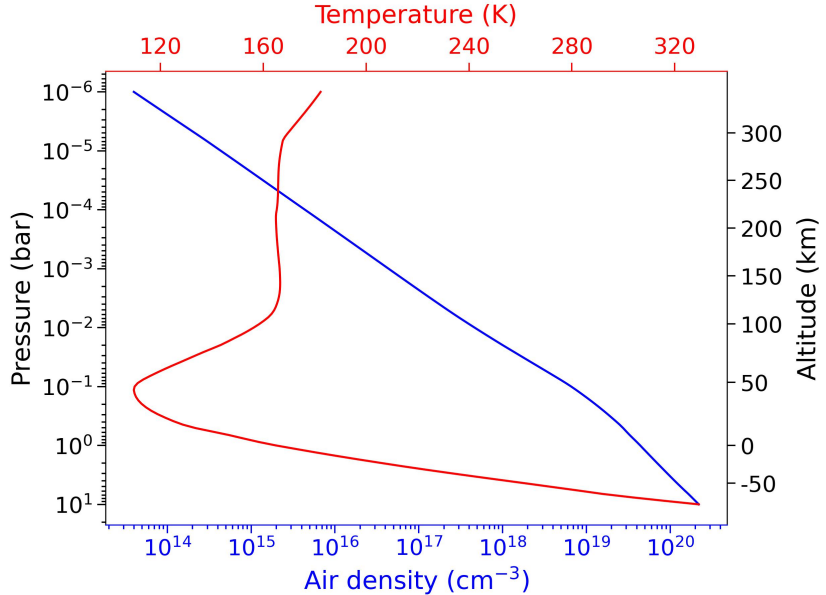


Figure 1: Profiles of temperature (red line) and particle number density (blue line) as a function of pressure and altitude in the GRS.

For the vertical profile of eddy diffusion  $K_{zz}(z)$  shown in Eq. 1, we adopted the formulation proposed by Irwin (2009):

$$K_{zz}(z) = \begin{cases} K_{zz}(z_H) \left[ \frac{N_H}{N(z)} \right]^\gamma, & \text{for } P \leq P_T \\ K_{zz}(z_T) \left[ \frac{N(z)}{N_T} \right], & \text{for } P > P_T \end{cases} \quad (2)$$

where  $P_T$  is the pressure at the tropopause,  $N(z)$  is the air number density, and  $N_H$  is the density at the homopause (defined as the altitude below which eddy mixing dominates over molecular diffusion).  $K_{zz}(z_H)$  is the associated eddy diffusion coefficient,  $N_T$  is the density at the tropopause, and  $\gamma$  is a dimensionless exponent typically close to 0.5. The vertical diffusion profile used in this work is shown in Fig. 2, computed assuming  $K_{zz}(z_H) = 1.4 \times$

$10^6 \text{ cm}^2 \text{ s}^{-1}$  (Irwin, 2009; Gladstone et al., 1996),  $K_{zz}(z_T) = 1.1 \times 10^4 \text{ cm}^2 \text{ s}^{-1}$  (Moses et al., 2005),  $N_H = 1.4 \times 10^{13} \text{ cm}^{-3}$  (Irwin, 2009; Gladstone et al., 1996),  $N_T = 6.59 \times 10^{18} \text{ cm}^{-3}$  (our calculated value at the tropopause, i.e., at 0.1 bar), and  $\gamma = 0.45$  (Gladstone et al., 1996).

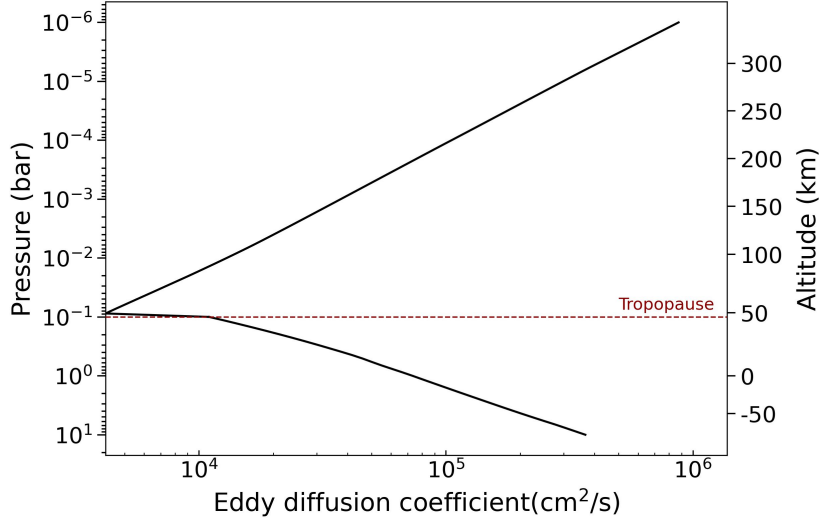


Figure 2: Vertical profile of the eddy diffusion coefficient used for the GRS.

According to Kasten (1968), the sedimentation velocity  $v_{\text{fall}}$  of a spherical particle with radius  $r$  and density  $\rho_p$ , falling through a medium with gravitational acceleration  $g$  and dynamic viscosity  $\eta$ , is given by:

$$v_{\text{fall}} = \frac{2}{9} \cdot \frac{\rho_p r^2 g}{\eta} [1 + A K_n + B K_n e^{-C/K_n}] \quad (3)$$

Here,  $K_n$  is the Knudsen number, a dimensionless parameter that characterizes whether the gas-particle interaction is in the continuum regime ( $K_n \ll 1$ ) or in the molecular (free molecular) regime ( $K_n \gg 1$ ) described by Maxwell-Boltzmann statistics. It is defined as

$$K_n = \frac{\lambda_g}{r}, \quad (4)$$

where  $\lambda_g$  is the gas mean free path and  $r$  is the particle radius. The sedimentation velocity formulation in Eq. 3 is valid across the full range of Knudsen numbers, smoothly bridging the continuum and free molecular regimes. The

correction factor in brackets accounts for slip-flow effects through a semi-empirical expression involving dimensionless coefficients  $A$ ,  $B$ , and  $C$ . In this work, we adopt the values  $A = 1.257$ ,  $B = 0.4$  and  $C = 1.1$  used in Chatterjee et al. (1975) and Sitarski & Seinfeld (1977), as discussed and justified in Pruppacher and Klett (2010). To characterize the dynamic viscosity  $\eta$  in the Jovian atmosphere, we adopted the profile given by Hansen (1979), which assumes a composition of 89%  $\text{H}_2$  and 11%  $\text{He}$  and depends only on temperature. Figure 3 shows the sedimentation velocities for particles with radii between 0.01 and 10  $\mu\text{m}$  in the GRS, assuming a particle density of  $\rho_p = 0.7 \text{ g/cm}^3$  (see Section 2.4 for our choice of this value). For particles with radius  $r = 0.1 \mu\text{m}$ , the sedimentation timescale at 0.1 bar, defined as  $\tau_{\text{fall}} = H/v_{\text{fall}}$  with  $H$  the local scale height, is approximately 12 yr, comparable to a Jovian year.

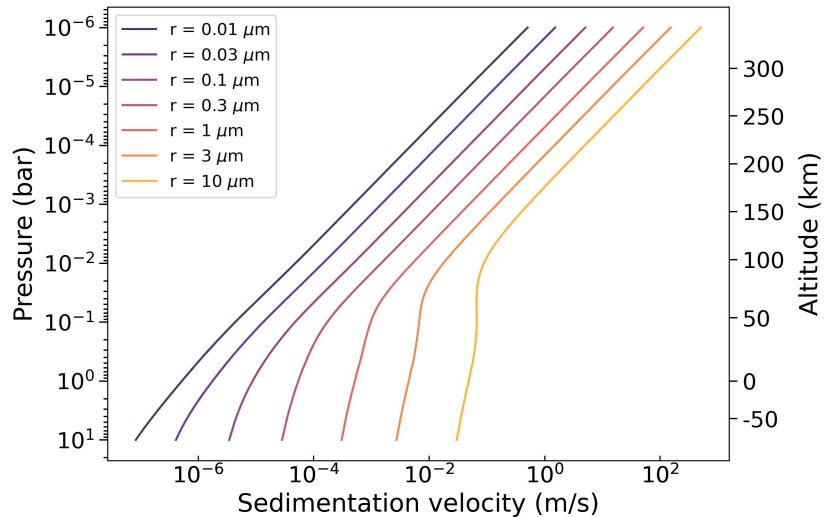


Figure 3: Sedimentation velocities for particles with radii in the range 0.01–10  $\mu\text{m}$  in the GRS according to the formulation of Kasten (1968).

The coagulation production and loss terms,  $P_{\text{coag}}$  and  $L_{\text{coag}}$ , in Eq. 1 are governed by the coagulation kernel  $K_{\text{coag}}(r_1, r_2)$  (Toon et al., 1988), which quantifies the rate at which particles of sizes  $r_1$  and  $r_2$  collide and stick together as a consequence of random thermal Brownian motion. In this work, we adopt the formulation of Sitarski & Seinfeld (1977), originally developed by Fuchs (1964). Given the length of the full expression for the coagulation kernel, we refer the reader to Sitarski & Seinfeld (1977) for the

detailed formulation. Its key advantage is its applicability across all flow regimes—continuum, transition, and free molecular. This is illustrated in Figure 4, in which the ratio of the Fuchs coagulation kernel to the Smoluchowski coagulation constant (Sitarzki & Seinfeld, 1977) is shown as a function of the Knudsen number.

For charged particles, the coagulation kernel is scaled by the sticking efficiency  $\alpha_s$ , defined as (Pollack et al., 1987):

$$\alpha_s = \exp\left(\frac{-k_C Q^2 e^2 r_1 r_2}{k_B T(r_1 + r_2)}\right), \quad (5)$$

where  $k_C = 1/(4\pi\varepsilon_0)$  is the Coulomb constant,  $Q$  is the number of elementary charges  $e$  per micron of radius,  $r_1$  and  $r_2$  the radii of the interacting particles,  $k_B$  the Boltzmann constant, and  $T$  the atmospheric temperature. This coefficient accounts for the electrostatic repulsion between like-charged particles, which reduces their probability of coagulating. Although explicit mention of the Coulomb constant  $k_C$  is typically absent from earlier formulations, its inclusion is required by dimensional analysis. This has been validated by comparison with the sticking efficiencies reported by Toon et al. (1980) for the cases of single-charged particles of size  $10^{-3}$ ,  $10^{-2}$ , and  $10^{-1}$   $\mu\text{m}$ .

### 2.3. Constraints from Radiative Transfer modelling

In our microphysical simulations, we aim to reproduce the values derived for the GRS, particularly the mass column density and the effective radius of the chromophore particles. These quantities have been constrained in previous studies, including Baines et al. (2019), Braude et al. (2020), and Anguiano-Arteaga et al. (2021, 2023). Significantly, there is an excellent agreement between the estimates of Baines et al. (2019) and Anguiano-Arteaga et al. (2021) for the chromophore mass column density in the GRS, both reporting values around  $30 \mu\text{g}/\text{cm}^2$ . A very similar value is found in the second preferred model of Braude et al. (2020), which yields effective radii more consistent with those from the other two studies. Across all these works focused on the GRS, the retrieved effective radii for the chromophore are of the order of a few tenths of a micron. This size range is likewise typical in the other radiative transfer studies discussed above.

We will therefore focus on the simulations showing a mass column density in the uncertainty range constrained by the minimum value of  $20 \mu\text{g}/\text{cm}^2$  reported by Anguiano-Arteaga et al. (2021) for the GRS nucleus and the maximum of  $40 \mu\text{g}/\text{cm}^2$  obtained by Baines et al. (2019) for a vertically extended

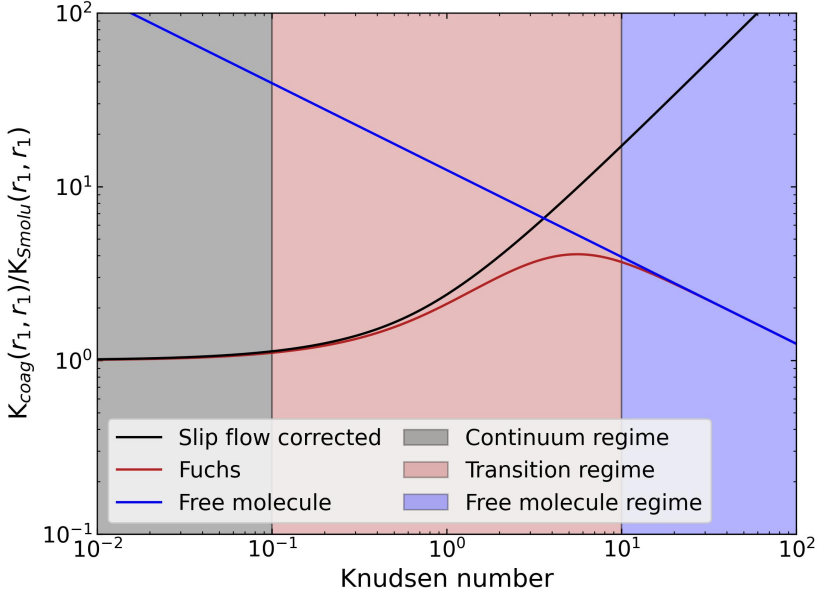


Figure 4: Ratio between the coagulation kernel  $K_{\text{coag}}(r_1, r_1)$  and the classical Smoluchowski constant  $K_{\text{Smolu}}(r_1, r_1)$  as a function of the Knudsen number, computed under terrestrial conditions ( $T = 298$  K,  $\eta = 1.85 \times 10^{-5}$  Pa · s, mean free path  $\lambda = 6.86 \times 10^{-8}$  m). The black line corresponds to the continuum regime with slip-flow corrections, the red line represents the Fuchs formulation, and the blue line indicates the free-molecule limit. Shaded regions highlight the continuum, transition, and free molecular regimes.

haze layer. As for the effective radius, we will consider simulations resulting in the range 0.2–0.35  $\mu\text{m}$  from the values reported by [Anguiano-Arteaga et al. \(2023\)](#). Notably, this study includes data from UV filters, which are particularly sensitive to particles of that size and to haze altitudes at the expected chromophore pressure levels ([Pérez-Hoyos et al. 2012](#), [Sánchez-Lavega et al. 2013](#)). Both the mass column density and the effective radius will be computed for pressures lower than 0.2 bar, corresponding to the chromophore pressure level reported by [Sromovsky et al. \(2017\)](#), [Baines et al. \(2019\)](#), and [Braude et al. \(2020\)](#). This range also includes the base pressure level of the chromophore layer, around 0.1 bar, as indicated by [Anguiano-Arteaga et al. \(2021\)](#).

## 2.4. Model parameters

To reproduce the retrieved properties of the chromophore layer in the GRS, we adopt a simplified yet physically motivated parameterisation of the microphysical model. The model is integrated on a one-dimensional vertical grid spanning pressures from 1 to  $10^{-3}$  bar (0–160 km), discretised into 52 layers approximately equally spaced in log-pressure. Particles are injected at a constant rate following a Gaussian distribution in pressure (Toon et al., 1980; Moreno, 1996), for which we explore different Full Width at Half Maximum (FWHM) values. In pressure coordinates, the vertical profile of the injection rate is prescribed as

$$C_{\text{inj}}(P) = C_{\text{inj}} \exp \left[ -\frac{(P - P_{\text{inj}})^2}{2\sigma^2} \right], \quad (6)$$

where  $P$  is the pressure,  $P_{\text{inj}}$  is the peak injection pressure, and  $C_{\text{inj}}$  denotes the peak injection rate (at  $P_{\text{inj}}$ ). The standard deviation  $\sigma$  is related to the FWHM via

$$\sigma = \frac{\text{FWHM}}{2\sqrt{2 \ln 2}}. \quad (7)$$

This injection, represented by the source term  $C_{\text{inj}}(z, r)$  in Eq. (1), is treated as local production of chromophore particles, with no explicit inflow from the domain boundaries. The injected particle size is fixed at  $0.01 \mu\text{m}$ , following Pollack et al. (1987) and as done by Moreno (1996) for the Jovian atmosphere. Individual molecules of the chromophore family identified by Carlson et al. (2016) have characteristic sizes of several angstroms, and in some cases, particularly those containing aromatic rings or extended hydrocarbon chains, are on the order of a nanometre. By adopting a minimum particle radius of  $0.01 \mu\text{m}$ , we ensure that the smallest size bin corresponds to aggregates comprising enough molecules for their geometry to be reasonably approximated as spherical. A constant upward vertical velocity, consistent with lower-limit estimates reported by Conrath et al. (1981), is imposed throughout the troposphere, i.e., the same value at all pressure levels below 100 mbar. The particle density is assumed to be  $0.7 \text{ g/cm}^3$ , based on the value for HCN reported in Haynes (2011), and similar to the hydrocarbon densities considered by Pollack et al. (1987) and Toledo et al. (2019).

To ensure numerical stability, we use an implicit time integration scheme, which is not limited by the Courant–Friedrichs–Lewy stability condition that constrains explicit schemes (Press et al., 1992). We adopt a fixed integration

time step of  $10^4$  s, consistent with the initial value used by [Pollack et al. \(1987\)](#). Numerical integrity is verified during the simulations by monitoring for the appearance of negative values, the absence of spurious numerical oscillations, and the expected evolution of the system's total mass. This allows for computationally efficient simulations over physically meaningful integration times. The simulations are run over a total integration time of almost 15 simulated terrestrial years, slightly more than one Jovian year, after which the effective radius and the mass column density are evaluated for convergence towards a steady state.

In order to constrain the microphysical parameters of the chromophore layer in the GRS, we explored a comprehensive grid of 2,160 models defined by five free parameters: the peak particle injection rate  $C_{\text{inj}}$ , the upward tropospheric velocity  $v_{\text{trop}}$ , the injection pressure level  $P_{\text{inj}}$ , the FWHM of the injection profile, and the number of electrons per micron of radius  $Q$ .

The vertical velocity range,  $v_{\text{trop}} \in [5.0 \times 10^{-5}, 1.0 \times 10^{-2}] \text{ m s}^{-1}$ , was chosen based on dynamical constraints. The lower limit is motivated by the estimate of  $v \geq 4.5 \times 10^{-5} \text{ m s}^{-1}$  at the GRS tropopause by [Conrath et al. \(1981\)](#), while the upper limit corresponds to the velocity required to fully suspend particles with radii up to  $3 \mu\text{m}$ , resulting in long convergence times exceeding 20 years. Within this range, six values were explored, evenly spaced in logarithmic scale.

Particle injection profiles (Eq. 6) were centred at two pressure levels, 0.1 and 0.2 bar, following the chromophore layer locations inferred by [Baines et al. \(2019\)](#), [Braude et al. \(2020\)](#), and [Anguiano-Arteaga et al. \(2021, 2023\)](#). Higher injection levels were excluded, as ammonia (a key precursor in the Carlson chromophore pathway) is significantly depleted above these pressures. The width of the injection profile, defined by its FWHM (Eq. 7), was varied between 30%, 60%, and 90% of the peak injection pressure. This choice spans relatively narrow and broad cases while avoiding excessive stratospheric injection. Expressing the FWHM as a fraction of the peak injection pressure allows the vertically integrated injection rate to remain comparable between profiles centred at 0.1 and 0.2 bar for a given peak value of  $C_{\text{inj}}$ .

The peak particle injection rate spanned from  $7.0 \times 10^{-3}$  to  $10 \text{ particles cm}^{-3} \text{ s}^{-1}$ . The lower bound corresponds to a scenario where a FWHM of 90% of  $P_{\text{inj}}$  yields a total mass column density of  $20 \mu\text{g/cm}^2$  over the simulation time, matching our lower acceptable limit. The upper bound leads to  $30 \mu\text{g/cm}^2$  being injected in just 20 days, ensuring that fast-growing scenarios are also captured. A total of ten values were explored, distributed logarithmically

within the range.

Finally, particle charge was varied between 5 and 30 electrons per micron of radius, in increments of 5. This range was selected based on an extensive preliminary analysis of more than a thousand simulations indicating that values above  $Q = 0$  electrons/ $\mu\text{m}$  were required to avoid excessively large effective radii at the target mass column densities. The upper limit of  $Q = 30$  electrons/ $\mu\text{m}$  is based on the value reported by [Moreno \(1996\)](#) for polar latitudes.

### 3. Results

Figure 5 shows a representative subset of the simulated cases, shown in terms of their output effective radius and mass column density (MCD). To enhance visual clarity, only a selection of the full grid is plotted, focusing on the region that spans the target ranges of  $r_{\text{eff}}$  and MCD defined in the previous section. A summary of the simulations that satisfy both constraints is provided in Table 1, where the optical depths ( $\tau$ ) were computed using the real and imaginary refractive indices used by [Anguiano-Arteaga et al. \(2021\)](#). The convergence time reported for each case is defined as the earliest simulation time at which both the effective radius and mass column density vary by less than 0.5% across five consecutive output points, sampled every 1,000 time steps.

Across the subset of cases that simultaneously fall within the observationally inferred ranges for  $r_{\text{eff}}$  ( $\sim 0.2$ – $0.35$   $\mu\text{m}$ ) and MCD ( $20$ – $40$   $\mu\text{g}/\text{cm}^2$ ), the convergence times are never shorter than  $\sim 7$  Earth years. We therefore identify this  $\sim 7$  years as a lower bound on the characteristic build-up time of the observed chromophore layer in the GRS. Faster-growing cases cannot match the required  $r_{\text{eff}}$  and MCD simultaneously.

These viable cases occupy a restricted region of the parameter space, with injection rates in the range  $C_{\text{inj}} \in [1.6 \times 10^{-2}, 4.0 \times 10^{-1}] \text{ cm}^{-3} \text{ s}^{-1}$ . Assuming a particle density of  $0.7 \text{ g cm}^{-3}$ , the corresponding volumetric mass injection rates span  $4.7 \times 10^{-17}$  to  $1.2 \times 10^{-15} \text{ kg m}^{-3} \text{ s}^{-1}$ ; when integrated over altitude, the associated column mass injection fluxes are  $1.1 \times 10^{-12}$  to  $6.9 \times 10^{-12} \text{ kg m}^{-2} \text{ s}^{-1}$ . Vertical velocities associated with these cases lie in the range  $v_{\text{trop}} \in [5.0 \times 10^{-5}, 1.4 \times 10^{-4}] \text{ m s}^{-1}$ , close to the lower bound estimated for the GRS tropopause by [Conrath et al. \(1981\)](#). Higher values of  $C_{\text{inj}}$  lead to shorter convergence times, as coagulation proceeds more rapidly when a greater number of particles is available. Conversely, higher values

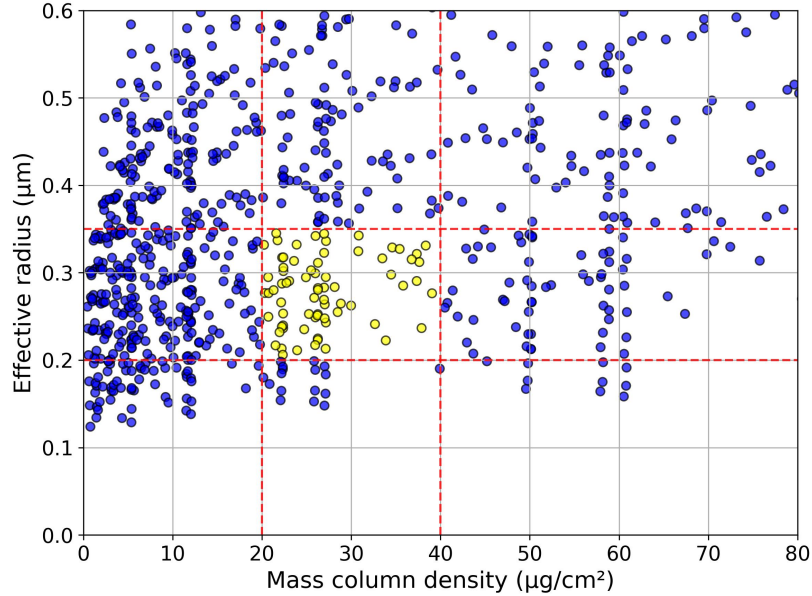


Figure 5: Output effective radius and mass column density for a subset of the simulated cases. Red dashed lines indicate the target ranges used to select viable models. Yellow points correspond to simulations that simultaneously meet both criteria. Only a portion of the full simulation set is shown for visual clarity.

of  $v_{\text{trop}}$  generally result in longer convergence times, given the higher fall velocity (and thus, size) needed for the particles to settle.

All simulations that satisfy the modelling constraints favour particle charge values of  $Q \geq 20$  electrons/ $\mu\text{m}$ , highlighting the importance of electrostatic repulsion in regulating coagulation and preventing excessive particle growth. As seen in Table 1, longest convergence times occur for  $Q = 30$  electrons/ $\mu\text{m}$ . However, this value does not necessarily imply a slow approach to a stationary state, with  $C_{\text{inj}}$  and  $v_{\text{trop}}$  being more decisive. As for the injection pressure, both tested levels—0.1 and 0.2 bar—are found to produce acceptable outcomes across all three FWHM values (30%, 60%, and 90% of the injection pressure), indicating that a variety of vertical injection profiles can lead to consistent simulations, provided that the injection remains within the chromophore region.

The P-T profile shown in Figure 1, as explained in Section 2.2, was constructed by averaging over a  $3 \times 3$  pixel region within the GRS’s reddish area. Given the spatial resolution of the temperature maps in Fletcher et

Table 1: Subset of simulations that meet the target ranges for output effective radius and mass column density.

$C_{\text{inj}}$ (particles $\text{cm}^{-3} \text{s}^{-1}$ )	$v_{\text{trop}}$ ( $\text{m s}^{-1}$ )	$P_{\text{inj}}$ (bar)	FWHM (bar)	$Q$ (electrons/ $\mu\text{m}$ )	$r_{\text{eff}}$ ( $\mu\text{m}$ )	MCD ( $\mu\text{g/cm}^2$ )	$\tau$ @ 900 nm	$t_{\text{conv}}$ (years)
$1.6 \times 10^{-2}$	$1.4 \times 10^{-4}$	0.1	0.09	30	0.22	21	1.40	14.3
$3.5 \times 10^{-2}$	$5.0 \times 10^{-5}$	0.1	0.09	20	0.33	24	2.21	8.9
$3.5 \times 10^{-2}$	$5.0 \times 10^{-5}$	0.1	0.09	25	0.28	28	2.40	9.8
$3.5 \times 10^{-2}$	$5.0 \times 10^{-5}$	0.1	0.09	30	0.24	33	2.40	10.8
$3.5 \times 10^{-2}$	$5.0 \times 10^{-5}$	0.2	0.18	25	0.25	21	1.54	10.1
$3.5 \times 10^{-2}$	$5.0 \times 10^{-5}$	0.2	0.18	30	0.21	24	1.43	11.4
$3.5 \times 10^{-2}$	$1.4 \times 10^{-4}$	0.1	0.09	20	0.34	31	2.92	9.8
$3.5 \times 10^{-2}$	$1.4 \times 10^{-4}$	0.1	0.09	25	0.29	37	3.31	11.4
$3.5 \times 10^{-2}$	$1.4 \times 10^{-4}$	0.2	0.18	20	0.31	24	2.12	10.8
$3.5 \times 10^{-2}$	$1.4 \times 10^{-4}$	0.2	0.18	25	0.26	29	2.30	12.0
$3.5 \times 10^{-2}$	$1.4 \times 10^{-4}$	0.2	0.18	30	0.22	34	2.21	13.6
$7.9 \times 10^{-2}$	$5.0 \times 10^{-5}$	0.1	0.06	20	0.34	22	1.97	7.3
$7.9 \times 10^{-2}$	$5.0 \times 10^{-5}$	0.1	0.06	25	0.29	25	2.14	7.9
$7.9 \times 10^{-2}$	$5.0 \times 10^{-5}$	0.1	0.06	30	0.25	28	2.19	8.6
$7.9 \times 10^{-2}$	$5.0 \times 10^{-5}$	0.2	0.18	20	0.33	35	3.14	8.2
$7.9 \times 10^{-2}$	$1.4 \times 10^{-4}$	0.1	0.06	25	0.32	33	3.03	10.1
$7.9 \times 10^{-2}$	$1.4 \times 10^{-4}$	0.1	0.06	30	0.28	39	3.27	11.1
$7.9 \times 10^{-2}$	$1.4 \times 10^{-4}$	0.2	0.12	25	0.29	21	1.74	11.4
$7.9 \times 10^{-2}$	$1.4 \times 10^{-4}$	0.2	0.12	30	0.25	25	1.91	12.7
$1.8 \times 10^{-1}$	$5.0 \times 10^{-5}$	0.1	0.03	20	0.33	20	1.81	7.6
$1.8 \times 10^{-1}$	$5.0 \times 10^{-5}$	0.1	0.03	25	0.29	23	1.94	8.2
$1.8 \times 10^{-1}$	$5.0 \times 10^{-5}$	0.1	0.03	30	0.25	26	1.96	8.9
$1.8 \times 10^{-1}$	$5.0 \times 10^{-5}$	0.2	0.12	20	0.35	22	1.90	7.3
$1.8 \times 10^{-1}$	$5.0 \times 10^{-5}$	0.2	0.12	25	0.30	26	2.14	8.2
$1.8 \times 10^{-1}$	$5.0 \times 10^{-5}$	0.2	0.12	30	0.26	30	2.28	9.2
$1.8 \times 10^{-1}$	$1.4 \times 10^{-4}$	0.1	0.03	25	0.32	31	2.77	10.1
$1.8 \times 10^{-1}$	$1.4 \times 10^{-4}$	0.1	0.03	30	0.29	36	3.02	11.1
$1.8 \times 10^{-1}$	$1.4 \times 10^{-4}$	0.2	0.06	25	0.28	20	1.63	10.8
$1.8 \times 10^{-1}$	$1.4 \times 10^{-4}$	0.2	0.06	30	0.23	25	1.72	12.4
$1.8 \times 10^{-1}$	$1.4 \times 10^{-4}$	0.2	0.12	25	0.33	38	3.35	10.1
$4.0 \times 10^{-1}$	$5.0 \times 10^{-5}$	0.2	0.06	25	0.29	23	1.85	7.9
$4.0 \times 10^{-1}$	$5.0 \times 10^{-5}$	0.2	0.06	30	0.25	27	1.94	8.9
$4.0 \times 10^{-1}$	$1.4 \times 10^{-4}$	0.2	0.06	25	0.31	38	3.21	9.5

al. (2020), this region encompasses both the GRS nucleus and its reddish surroundings. To select a representative simulation, we adopted as benchmarks the averages reported by Anguiano-Arteaga et al. (2021) for those two regions:  $r_{\text{eff}} = 0.31 \mu\text{m}$ , MCD =  $25 \mu\text{g cm}^{-2}$ , and  $\tau(900 \text{ nm}) = 2.15$ . The simulation that most closely matches these targets corresponds to an injection rate of  $C_{\text{inj}} = 3.5 \times 10^{-2} \text{ cm}^{-3} \text{s}^{-1}$ , a vertical tropospheric velocity of  $v_{\text{trop}} = 1.4 \times 10^{-4} \text{ m s}^{-1}$ , an injection pressure of 0.2 bar, a FWHM of 0.18 bar, and a particle charge of  $Q = 20 \text{ electrons}/\mu\text{m}$ . The temporal evolution of the effective radius and mass column density for this reference case is shown in Figure 6. Both quantities progressively increase and con-

verge toward steady values after approximately 11 years of simulated time, indicating that the system reaches equilibrium on that timescale. The cumulative optical depths spanned by the successful simulations in Table 1, together with the corresponding curve of the reference case and the analogous chromophore profiles retrieved from radiative transfer modelling by [Anguiano-Arteaga et al. \(2021\)](#) for the GRS nucleus and its surrounding reddish interior, are shown in Figure 7. The vertical and size distribution of particles at different stages of the reference simulation is presented in Figure 8, where the growth by coagulation and sedimentation of larger particles can be observed, along with upward diffusive transport. This interplay of microphysical processes leads to a vertically extended haze structure with a broad particle size range, stabilizing over time. Some of the characteristic features of this type of simulation, together with its physical plausibility and relevance to previous radiative transfer modelling results, are discussed in the following section.

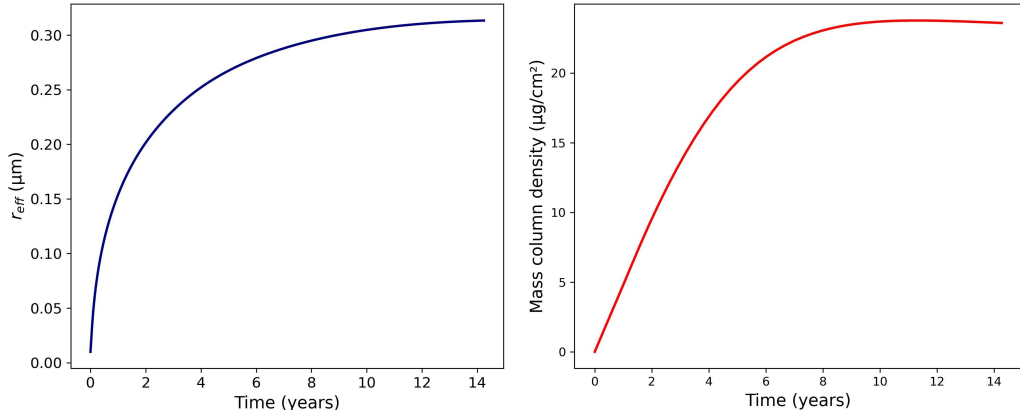


Figure 6: Time evolution of the effective radius (left) and mass column density (right) for the selected model. Both properties asymptotically approach a stationary state after approximately a Jovian year ( $\approx 12$  terrestrial years).

## 4. Discussion

### 4.1. Origin of the GRS chromophore

In Figure 9, we compare the retrieved chromophore mass production profiles with the availability of parent gases. We compute the  $\text{C}_2\text{H}_2$  vertical flux divergence (i.e., the local rate of supply per unit volume) from

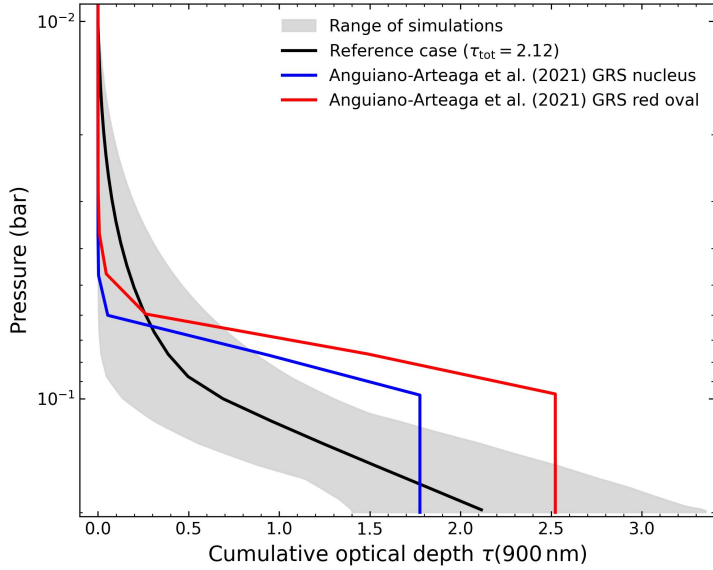


Figure 7: Cumulative optical depth at 900 nm as a function of pressure. The grey shaded region shows the range spanned by the successful microphysical simulations listed in Table 1, and the solid black line highlights the reference case. The blue and red curves show the chromophore profiles retrieved from radiative transfer modelling by [Anguiano-Arteaga et al. \(2021\)](#) for the GRS nucleus and its surrounding red oval, respectively. In those retrievals, the base of the chromophore layer lies near  $P = 0.1$  bar, so the cumulative optical depth remains approximately constant at higher pressures.

the flux in the supplementary material of [Moses et al. \(2010\)](#), and take the  $\text{NH}_3$  photodissociation rate from [Cheng et al. \(2006\)](#). In constructing the available mass curve below the tropopause, where  $\text{NH}_3$  remains abundant, we adopt the working assumption that two  $\text{NH}_3$  molecules are available per acetylene molecule, motivated by the two-N-bearing composition of the Carlson-type chromophores. Above the tropopause, however, ammonia scarcity may limit production. To preserve the two- $\text{NH}_3$  per unit interpretation without overspending  $\text{NH}_3$ , we enforce a limiting-reagent condition at each pressure: we compare the molecular supply of  $\text{C}_2\text{H}_2$  with half the molecular rate of  $\text{NH}_3$  and adopt the lower value. The resulting limiting molecular rate is then converted to mass by multiplying by the combined mass of one  $\text{C}_2\text{H}_2$  plus two  $\text{NH}_3$ , yielding an availability curve that is valid both below and above the tropopause. In addition, we derive an “enhanced” availability by computing an enhanced  $\text{C}_2\text{H}_2$  flux from the retrieved

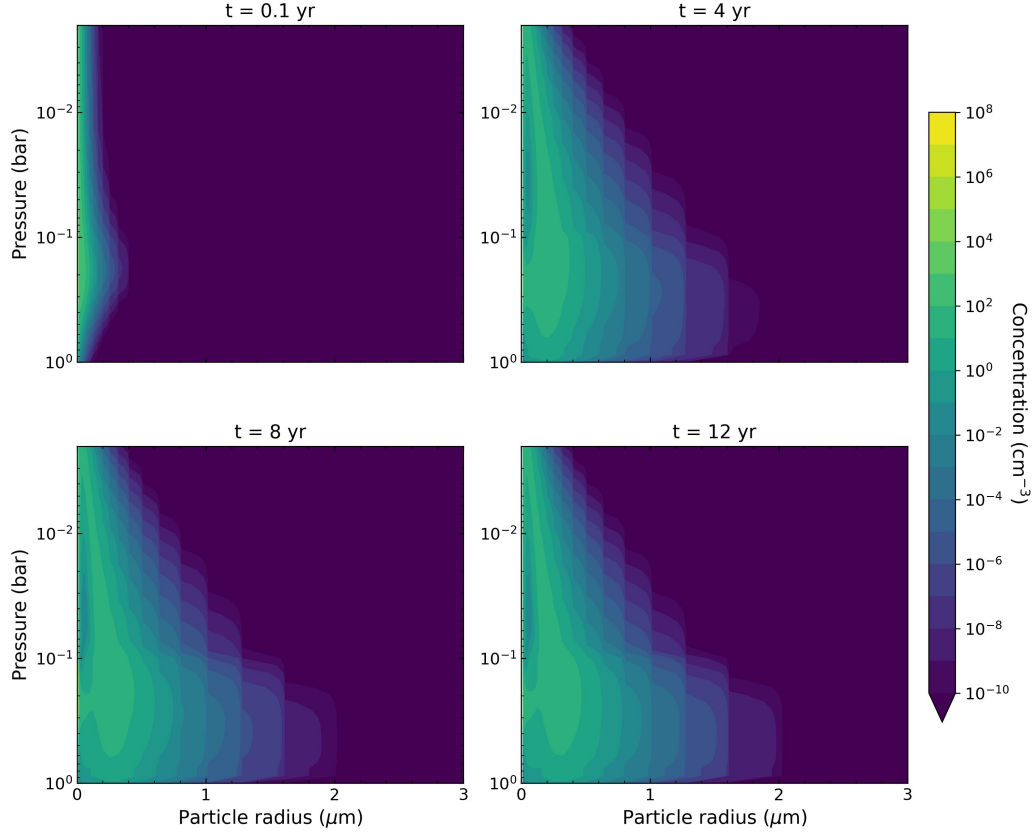


Figure 8: Temporal evolution of the particle size distribution and vertical concentration profile at four selected times (0.1, 4, 8, and 12 years). Each panel shows the concentration as a function of particle radius and pressure.

mole-fraction ratio  $R(P) = f_{\text{enh}}/f_{\text{nom}}$  and a diffusive-transport adjustment,  $\Phi_{\text{enh}} = R \cdot \Phi_{\text{nom}} - K_{zz} \cdot N \cdot f_{\text{nom}} \cdot dR/dz$ , where  $f_{\text{nom}}$  and  $f_{\text{enh}}$  are the nominal and lightning-enhanced  $\text{C}_2\text{H}_2$  mole fractions reported by [Moses et al. \(2010\)](#), respectively. We then take the vertical divergence of  $\Phi_{\text{enh}}$  under the same limiting-reagent assumption.

As can be seen from Figure 9, the successful simulations exceed the available mass for chromophore formation, with  $\text{C}_2\text{H}_2$  supply as the principal limiting factor in the troposphere. Furthermore, only a fraction of the available mass would be converted into chromophore material, depending on the chemical efficiency of the formation pathways. Using the available mass profile as the input injection profile in our microphysical model, we find that the

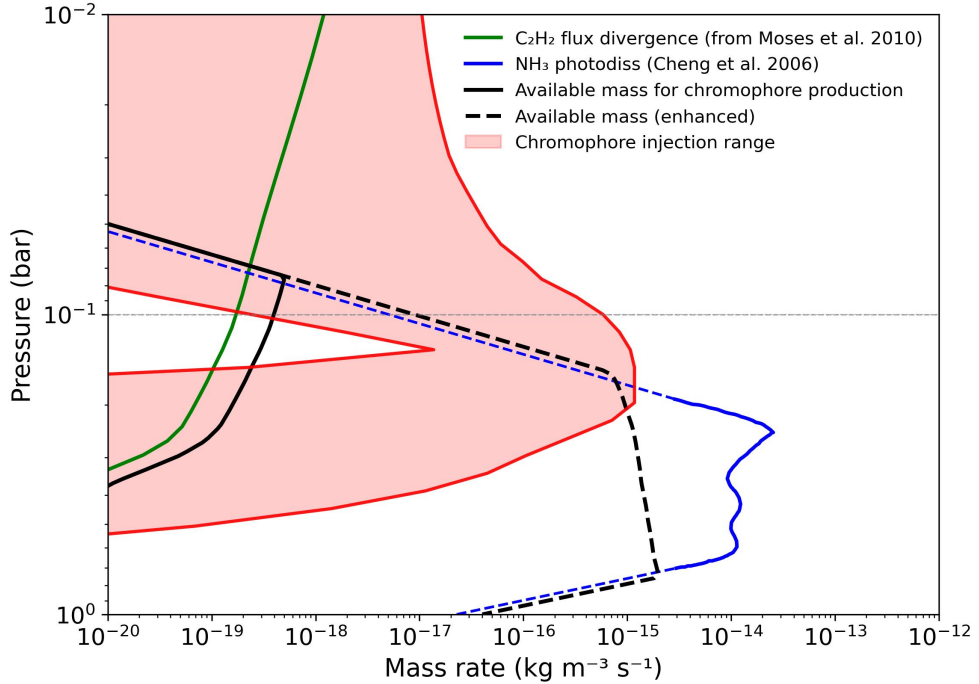


Figure 9: Comparison between retrieved chromophore mass production rates and the mass availability from parent gases. The green line shows the  $\text{C}_2\text{H}_2$  flux divergence from Moses et al. (2010), while the blue line corresponds to the  $\text{NH}_3$  photodissociation rate from Cheng et al. (2006), dashed segments showing extrapolated regions. The solid black curve is the nominal available mass for chromophore production; and the black dashed curve is the lightning-enhanced available mass. The shaded red region indicates the range of chromophore injection profiles consistent with our microphysical simulations.

system reaches a steady state after approximately 10–25 years (depending on the assumed  $v_{\text{trop}}$  and  $Q$ ), with a resulting chromophore mass column density of about  $0.1 \mu\text{g}/\text{cm}^2$ , well below the observational target range. When using an enhanced injection based on the lightning-enhanced  $\text{C}_2\text{H}_2$  case, the model outputs approach the observational target range: our closest overall match occurs for  $v_{\text{trop}} = 5 \times 10^{-5} \text{ m s}^{-1}$  and  $Q = 25 \text{ electrons}/\mu\text{m}$ , yielding  $r_{\text{eff}} = 0.35 \mu\text{m}$ ,  $\text{MCD} = 41 \mu\text{g}/\text{cm}^2$  and a convergence time of approximately 6 years. Simulations that fall within the desired  $r_{\text{eff}}$  and  $\text{MCD}$  ranges are obtained for chemical efficiencies in the range of 20–95% in  $\sim 7\text{--}12$  years. The plausibility of a  $\text{C}_2\text{H}_2$  enhancement by lightning remains debated (Moses et al., 2010; Baines et al., 2019). However,  $\text{C}_2\text{H}_2$  observational constraints

near and below the tropopause are sparse, and predicted abundances from different photochemical models often differ by more than an order of magnitude (Knížek et al., 2026). Comparatively large  $\text{C}_2\text{H}_2$  mole fractions, such as those reported by Bétrémieux et al. (2003), could meet the required production rates. Future work should therefore clarify whether tropospheric  $\text{C}_2\text{H}_2$  abundances in the GRS can significantly exceed current photochemical predictions for Jupiter.

As proposed by Carlson et al. (2016), an enhanced upward flux of  $\text{NH}_3$  into the high troposphere could increase the material available for chromophore formation. Enhanced injection at higher altitudes is compatible with our range of injection profiles in Fig. 9. However, current observations show no persistent, large-scale enhancement of  $\text{NH}_3$  in the upper troposphere of the Great Red Spot, as shown by recent analyses of JWST/MIRI (Harkett et al., 2024) and Juno/JIRAM data (Grassi et al., 2021).

Our study indicates that  $\text{C}_2\text{H}_2$  is the limiting reagent for chromophore formation at 0.1–0.2 bar. Various photochemical models of Jupiter predict a mole fraction of  $\sim 10^{-9}$  near the tropopause (Moses et al., 2005, 2010; Hue et al., 2018). We explore if other hydrocarbons, however, could also play a role. Models also predict mole fractions of  $\text{C}_2\text{H}_6$  that exceed that of  $\text{C}_2\text{H}_2$ , yet our analysis of flux divergences from Moses et al. (2010) shows that their local volumetric supply between 0.3 bar and 1 mbar are similar.  $\text{C}_2\text{H}_6$  is known to be less reactive than  $\text{C}_2\text{H}_2$ , and its photolysis also requires higher-energy photons, which penetrate less deeply. For the next most abundant hydrocarbon,  $\text{C}_2\text{H}_4$ , the flux divergence is two orders of magnitude lower. We therefore infer that the Carlson chromophore is unlikely to be sourced primarily from  $\text{C}_2\text{H}_4$  or  $\text{C}_2\text{H}_6$  at these levels. Secondary contributions, however, cannot be ruled out. Robust quantification would require a GRS-tailored photochemical model that considers all plausible pathways and realistic, potentially enhanced, vertical transport.

#### 4.2. Particle size and vertical distributions

In our simulations, the effective particle radius increases monotonically with pressure, as shown in Figure 10. A distinct change in curvature occurs near the tropopause as a consequence of the structure of the eddy diffusion coefficient profile  $K_{zz}$  (Figure 2). This change is not caused by the tropospheric vertical velocity, as it persists even when  $v_{trop}$  is set to zero, albeit yielding slightly smaller tropospheric particles. In our setup,  $K_{zz}$  reaches a minimum near the tropopause and then increases toward higher pressures.

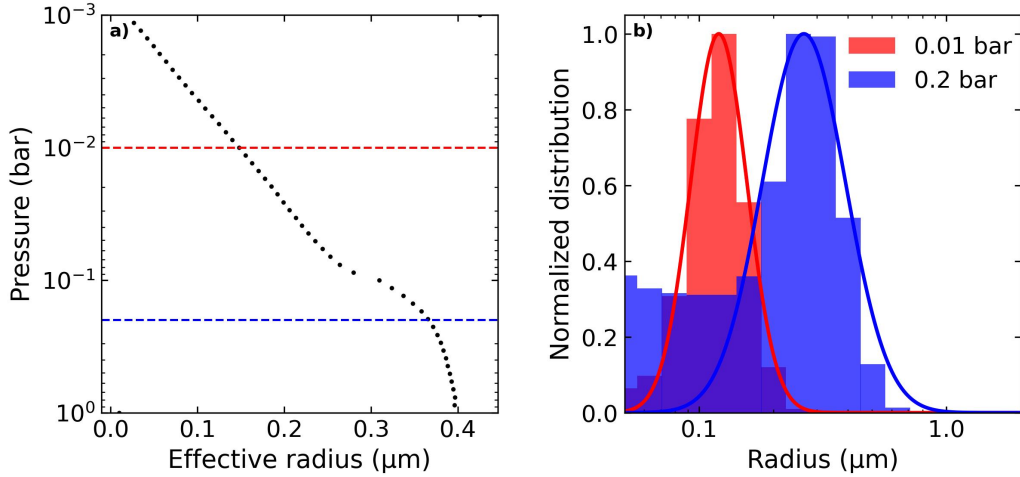


Figure 10: For the reference simulation: (a) Effective radius  $r_{\text{eff}}$  versus pressure; dashed lines mark the two selected pressure levels. (b) Normalized histograms (peak-normalized to 1) with a size cutoff  $r \geq 0.05 \mu\text{m}$  and the corresponding log-normal fit (solid line).

Since the residence time for collisional growth scales as  $\tau_{\text{mix}} \sim H^2/K_{zz}$  (with  $H$  a scale height), particles spend longer near this minimum and grow more efficiently there; as  $K_{zz}$  rises with depth,  $\tau_{\text{mix}}$  shortens and transport limits further growth, yielding the near-asymptotic behavior of  $r_{\text{eff}}$  at depth. With a constant-log-slope  $K_{zz}$  (decreasing with pressure),  $r_{\text{eff}}$  grows more steeply below the tropopause and approximately linearly with  $\log P$  and the near-asymptotic deep behavior no longer appears.

Figure 10 also shows particle size distributions at 0.01 bar and 0.2 bar. When the full size range is considered, the distributions peak at the minimum radius, reflecting the injected seed particles. However, these small particles contribute weakly to light extinction: more than 99% of total optical depth is due to particles with radii above 0.1  $\mu\text{m}$ . Motivated by this result, the right plot (panel b) excludes small particles and overlays fits to a log-normal distribution (Hansen & Travis, 1974). At 0.01 bar the particle size distribution is well described by a log-normal distribution, whereas at 0.2 bar the distribution exhibits a low-radius wing that a single log-normal cannot reproduce. This wing again reflects the behavior of  $K_{zz}$  in the troposphere: when  $K_{zz}$  is prescribed with a constant slope in  $\log P$ , the resulting distributions are well represented by a single log-normal. Despite the small-radius wing, the conventional log-normal assumption remains appropriate for radiative trans-

fer parameterizations, as extinction is dominated by larger particles: in our simulations, particles with  $r > 0.2 \mu\text{m}$  account for over 97% of the column optical depth.

A widely used parameterization in radiative transfer calculations is the Crème-Brûlée layout, in which the chromophore is located in a thin layer (extending from 0.20 to 0.18 bar) on top of the tropospheric ammonia cloud (Sromovsky et al., 2017; Baines et al., 2019). This scheme is not supported by our calculations. We tested chromophore configurations with very narrow injections near 0.20 bar and found that the layers broaden rapidly, as diffusion quickly smooths steep vertical gradients and spreads particles vertically. Consistent with this behavior, the optical depth in the models of Table 1 is not strongly concentrated in a thin sheet: only about 15% of the column optical depth arises from 0.20–0.18 bar, whereas typically more than 75% originates between 0.20 and 0.10 bar. Additional mechanisms that counteract the diffusive flux would be required to confine the particle concentration in narrow layers.

## 5. Conclusions

We have developed a one-dimensional microphysical model, based on the computational analogs of Toon et al. (1988), that includes sedimentation, eddy diffusion and coagulation. Using physically plausible parameters and realistic timescales, we have reproduced the effective radii and mass column densities inferred for the Carlson et al. (2016) chromophore in the Great Red Spot by recent radiative transfer studies (Baines et al., 2019; Braude et al., 2020; Anguiano-Arteaga et al., 2021). No condensational growth is needed to match these values. Our main conclusions are as follows:

- **Formation timescale.** For parameter combinations that reproduce the previously reported effective radii ( $\sim 0.2\text{--}0.35 \mu\text{m}$ ) and mass column densities ( $20\text{--}40 \mu\text{g/cm}^2$ ), the chromophore haze in the GRS requires at least 7 Earth years of continuous injection to approach steady state. This sets a lower bound on the characteristic formation time of the haze and provides the first quantitative constraint on the build-up timescale of the GRS chromophore.
- **Chromophore production rate.** The minimum column-integrated injection rate required by our successful models is  $\sim 10^{-12} \text{ kg m}^{-2} \text{ s}^{-1}$ .

The needed rates exceed the mass available from parent gases implied by photochemical models— $\text{C}_2\text{H}_2$  flux divergences from Moses et al. (2010) and  $\text{NH}_3$  photodissociation from Cheng et al. (2006). In the troposphere  $\text{C}_2\text{H}_2$  is the limiting reagent, whereas above the tropopause photolyzed  $\text{NH}_3$  limits production. This implies that higher  $\text{C}_2\text{H}_2$  tropospheric abundances and associated fluxes could meet the required budget. Notably, existing photochemical models are not GRS-specific, and observational constraints on  $\text{C}_2\text{H}_2$  at the relevant pressures ( $\sim 0.1$ – $0.2$  bar) remain sparse. As already pointed out by Baines et al. (2019), lightning–driven  $\text{C}_2\text{H}_2$  production (Bar-Nun & Podolak, 1985; Podolak & Bar-Nun, 1988) could provide such an enhancement. The JUICE mission is expected to deliver a statistical view of Jovian lightning activity across different atmospheric regions (Fletcher et al., 2023), offering a way to evaluate this possibility.

- **Size–distribution parameterization.** Above the optically relevant cutoff ( $r \gtrsim 0.1 \mu\text{m}$ ), the simulated particle size distributions are well represented by a single log–normal at the pressure levels that dominate extinction. A log–normal parameterization is therefore adequate for radiative transfer retrievals of the Carlson type chromophore.
- **Vertical layout.** A thin, Crème–Brûlée–type sheet confined to  $\sim 0.20$ – $0.18$  bar is not favored in our model: eddy diffusion rapidly broadens any narrowly injected layer, and the steady–state optical depth is vertically distributed rather than concentrated in a thin slab. Additional processes that counteract the diffusive flux would be required to maintain a persistent, sharply confined chromophore layer.

We identify three priorities to solidify the Carlson-type chromophore scenario. (i) Constrain the chromophore-production budget: measurements of  $\text{C}_2\text{H}_2$  mixing ratios at  $\sim 0.2$  bar and associated fluxes in the GRS are needed to test whether the  $\text{C}_2\text{H}_2$ –limited injection rates indicated in Figure 9 are achievable. A GRS-specific photochemical model, including accurate vertical transport and all plausible pathways to the Carlson-family compounds, would enable quantification of chromophore-production efficiencies under realistic conditions. Stratospheric  $\text{NH}_3$  measurements would help discern whether a portion of the chromophore is produced above the tropopause. As additional tracers, enhanced  $\text{HCN}$  and  $\text{CH}_3\text{CN}$  mixing ratios would be consistent with strengthened N-bearing photochemistry (Moses et al., 2010; Baines et al.,

2019). (ii) Radiative transfer modelling: our analysis builds on radiative transfer retrievals of the GRS, an intrinsically degenerate problem that affects estimates of the chromophore vertical location, size distribution, and abundance. Degeneracies can be mitigated by modelling spectra over an extended wavelength range, ideally from UV to thermal IR, at high spectral resolution and for multiple observing geometries. As an additional means of identifying the most probable parameter combinations defining vertical haze structure, Bayesian inference techniques have already been employed for Solar System giant planets (e.g. Uranus; [de Kleer et al., 2015](#)) and for exoplanets ([Roy-Perez et al., 2025](#)). Notably, the widely used NEMESIS radiative transfer suite ([Irwin et al., 2008](#)) now includes a Bayesian enabled implementation ([Alday et al., 2025](#)). (iii) Laboratory constraints: precise spectral modelling requires robust optical properties for Carlson-type materials, specifically tightly constrained complex refractive indices determined over the UV–IR range. In addition, because the Carlson family is broad, the subset of compounds whose spectra are compatible with Jovian absorption should be identified and prioritised.

### CRediT authorship contribution statement

**Asier Anguiano-Arteaga:** Conceptualization, Methodology, Software, Validation, Formal analysis, Investigation, Data curation, Visualization, Writing – original draft, Writing – review & editing.

**Santiago Pérez-Hoyos** Conceptualization, Supervision, Project administration, Funding acquisition, Methodology, Writing – review & editing.

**Agustín Sánchez-Lavega** Supervision, Project administration, Funding acquisition, Writing – review & editing.

**Patrick G.J. Irwin** Resources, Supervision, Writing – review & editing.

### Declaration of competing interest

The authors declare that they have no known competing financial interests or personal relationships that could have appeared to influence the work reported in this paper.

### Data availability

Data will be made available on request.

## Acknowledgments

We are very thankful to D. Toledo for insightful advice on microphysical modelling, including guidance on the treatment of haze formation and on the assessment of steady-state convergence.

This work was supported by the Basque Government (Grupos de Investigación, IT1742-22), Elkartek KK-2025/00106 and by Grant PID2023-149055NB-C31 funded by MICIU/AEI/10.13039/501100011033 and by FEDER, UE

A. Anguiano-Arteaga was supported by the *Programa de Perfeccionamiento de Personal Investigador Doctor 2024–2027* of the Basque Government.

## Appendix A. Validation of Computational Algorithms

In the absence of particle injection, Eq. 1 can be separated into:

$$\frac{\partial C(z, r)}{\partial t} - \frac{\partial [\rho \cdot K_{zz}(z)]}{\partial z} \cdot \frac{\partial}{\partial z} \left[ \frac{C(z, r)}{\rho} \right] + \frac{\partial [W(z, r) \cdot C(z, r)]}{\partial z} = 0 \quad (\text{A.1})$$

$$\frac{\partial C(z, r)}{\partial t} = P_{\text{coag}}(z, r) - L_{\text{coag}}(z, r) \quad (\text{A.2})$$

The first equation describes vertical transport (Eq. A.1), while the second governs the coagulation processes responsible for the production and loss of particles of a given size at a given altitude (Eq. A.2). As discussed by [Toon et al. \(1988\)](#), the vertical transport equation can be formulated in such a way that it allows for either an explicit or implicit numerical solution. In our implementation, we generally prefer the implicit approach, as it prevents negative concentrations and ensures numerical stability even when using relatively large time steps.

To validate our implementation of vertical transport, we compare its behavior against known analytical solutions, focusing on cases of pure diffusion, diffusion with advection, and pure advection.

In the case of pure diffusion, we compare our numerical results with the analytical solution to Eq. A.1, as presented by [Toon et al. \(1988\)](#):

$$\begin{aligned} C(t, z) = & C_0 / (2\sqrt{\pi K_{zz} t}) \left\{ \exp[-(z - z_0)^2 / (4K_{zz} t)] \right\} \\ & + \exp[-(z + z_0)^2 / (4K_{zz} t)] \\ & \cdot \exp[-W(z - z_0) / (2K_{zz}) - W^2 t / (4K_{zz})] \\ & + C_0 W \exp(-Wz / K_{zz}) / (K_{zz} \sqrt{\pi}) \\ & \cdot \int_{(z+z_0-Wt)/(2\sqrt{K_{zz}t})}^{\infty} e^{-\gamma^2} d\gamma \end{aligned} \quad (\text{A.3})$$

where  $C_0$  is the initial concentration, modeled as a Dirac delta function centered at altitude  $z_0$ . Note that  $\gamma$  is simply a variable of integration. We also corrected a typographical error in the equation as printed in [Toon et al. \(1988\)](#), where the coefficient should read  $2\sqrt{\pi K_{zz} t}$  instead of  $2\pi K_{zz} t$ ,

following the original form given in [Hidy and Brock \(2013\)](#), in which also appears an additional sign typo in the 1970 edition of the original source (where a ‘+’ sign mistakenly appears in the lower limit of the integral instead of a ‘-’).

When the atmospheric density is constant, Eq. [A.3](#) is directly applicable. However, if the density follows an exponential profile,  $\rho = \rho_0 e^{-z/H_\rho}$ , with constant scale height  $H_\rho$ , the solution remains valid by replacing  $W$  with  $K_{zz}/H_\rho$ . The excellent agreement with our model results, as illustrated in Figure [A.1](#), confirms the accuracy of the diffusion treatment. Please note that our solutions also show an excellent match to those of [Toon et al. \(1988\)](#).

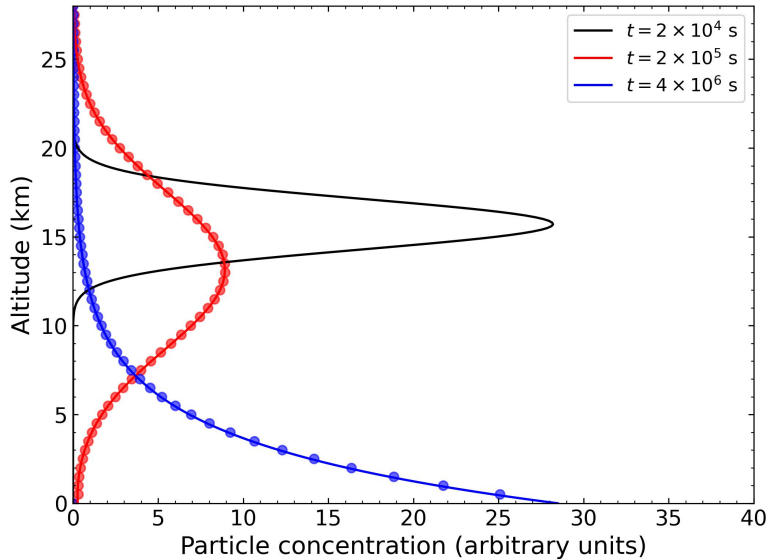


Figure A.1: Pure diffusion solution in an atmosphere with  $H_\rho = 3.5$  km, assuming a constant eddy diffusion coefficient of  $K_{zz} = 50$  m<sup>2</sup>/s. Solid lines correspond to the analytical solution from Eq. [A.3](#), while dots show the numerical results for different simulated times. The distribution corresponding to the earliest time represents the initial distribution in the numerical model.

To evaluate cases with both advection and diffusion, we follow the same procedure and use again Eq. [A.3](#), but replacing  $W$  with  $W + K_{zz}/H_\rho$ . This is shown in Figure [A.2](#), where the comparison between the analytical and numerical cases is performed for different combinations of  $W$  and  $K_{zz}$  values. The results of this comparison are again satisfactory, although a larger

discrepancy is observed in the case with the lowest diffusion ( $K_{zz} = 1 \text{ m}^2/\text{s}$ ), similarly to what was reported by [Toon et al. \(1988\)](#). This discrepancy arises primarily from numerical diffusion introduced by the advection scheme. While the technique proposed by [Toon et al. \(1988\)](#) to minimize numerical diffusion proves effective, it does not eliminate it entirely—particularly when the advection term  $W$  becomes significant relative to  $K_{zz}$ . In our model, however, the lowest  $K_{zz}$  values occur near the tropopause (see Figure 2), where sedimentation velocities tend to be small for typical particle sizes (see Figure 3), which rarely exceed radii of  $3 \mu\text{m}$  under typical conditions, as shown in Figure 8.

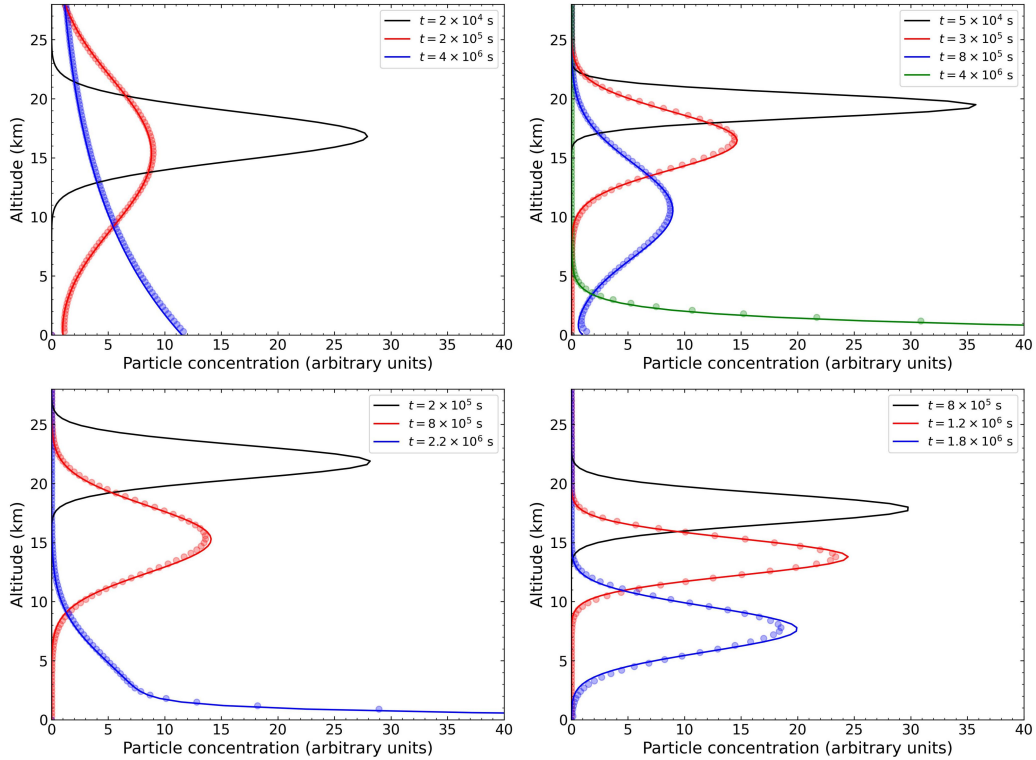


Figure A.2: Analytical solutions (solid lines) of the advection–diffusion equation in an atmosphere with  $H_\rho = 5.5 \text{ km}$  compared with the numerical model (dots) for the following cases: a)  $W = 0.01 \text{ m/s}$  and  $K_{zz} = 100 \text{ m}^2/\text{s}$ ; b)  $W = -0.01 \text{ m/s}$  and  $K_{zz} = 10 \text{ m}^2/\text{s}$ ; c)  $W = -0.01 \text{ m/s}$  and  $K_{zz} = 5 \text{ m}^2/\text{s}$ ; d)  $W = -0.01 \text{ m/s}$  and  $K_{zz} = 1 \text{ m}^2/\text{s}$ . The time step is  $10^4 \text{ s}$ . The values of  $W$  and  $K_{zz}$  were chosen to match those used in [Toon et al. \(1988\)](#). In each panel, the distribution corresponding to the earliest time represents the initial distribution in the numerical model.

The validation of the pure advection case is carried out by analyzing both the displacement and the shape of the initial concentration profile, after imposing vertical velocities of equal magnitude ( $|W| = 0.1 \text{ ms}^{-1}$ ) but in opposite directions. In a purely advective scenario, where particles move vertically at a constant speed, the initial distribution should ideally shift without undergoing any distortion. Figure A.3 presents the outcome of this test, showing that the initial profile experiences minimal distortion. This confirms that the model accurately represents advection and that the strategy implemented to suppress numerical diffusion is effective. Minor deviations in peak position relative to the expected displacement are not considered significant, as the velocities in the model are not known to such high precision, as pointed out by [Toon et al. \(1988\)](#). Furthermore, it should be noted that pure advection does not occur in Jupiter's atmosphere, where eddy diffusion is always present.

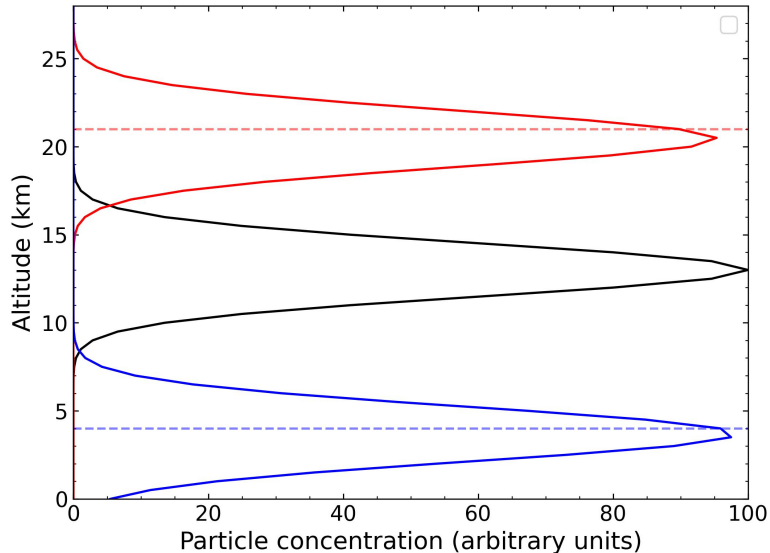


Figure A.3: Validation of the numerical code for the case of pure advection. The red curve corresponds to upward motion and the blue one to downward motion. The dashed lines indicate where the peaks of the same-colored curves should be found. In the ideal case, the shape of the initial distribution would not change and, as shown, the peaks exhibit little distortion.

To evaluate the coagulation scheme, we compare the model outputs with the analytical Smoluchowski solutions for an initially monodisperse aerosol

subject to a constant coagulation kernel (Friedlander, 2000), as introduced by Turco et al. (1979b) and later adopted by Toon et al. (1988). Starting from a single particle in the first size bin, we track particle population evolution in terms of the characteristic coagulation time  $\tau_0$ , as defined by Friedlander (2000). The results are shown in Figures A.4 and A.5, where good agreement is observed between the model and the analytical solutions.

Figure A.4 shows the temporal evolution of the total number of particles and those remaining in the first size bin. The total particle number decreases over time because multiple particles must combine to form larger aggregates. However, mass (or volume equivalently, as we assume constant particle density) is conserved throughout the simulation. Figure A.5 presents the bin-population distribution at different coagulation times. Minor discrepancies between the numerical and analytical results arise from the transformation of the classical linearly spaced volume bins in the Smoluchowski solution into the geometrically increasing bins used in our model, following the procedure outlined by Turco et al. (1979b), whose results also display similar differences. These deviations are attributable to binning artifacts rather than inaccuracies in the model, as can be inferred from the excellent agreement shown in Figure A.4, the non-smooth appearance of the analytical Smoluchowski curves in Figure A.5 and by the fact that any mismatch observed at a given time does not propagate to subsequent time steps. As a final validation check, we have confirmed that the model conserves the total mass column density when both vertical transport and coagulation are active. In the presence of particle injection, the mass column density increases linearly in accordance with the specified injection rate.

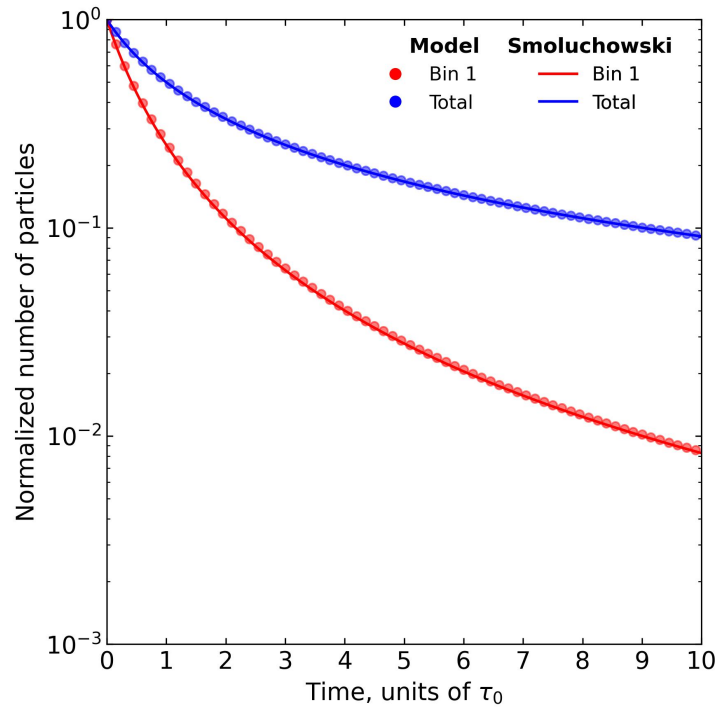


Figure A.4: Temporal evolution of the total number of particles and those remaining in the first size bin, comparing the numerical model with the analytical Smoluchowski solution. The decrease in particle number reflects the effects of coagulation. Mass is conserved throughout the simulation.

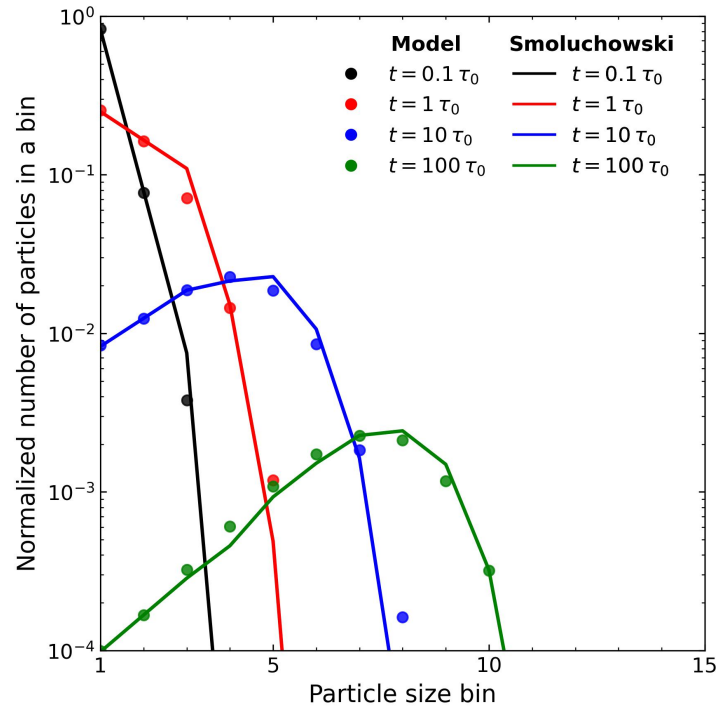


Figure A.5: Evolution of the particle size spectrum over time, comparing the numerical model with the analytical Smoluchowski solution. Small deviations and the non-smooth Smoluchowski curves originate from translating the linearly spaced volume bins used in the analytical solution onto the model's geometrically spaced volume bins.

## References

Alday, J., Penn, J., Irwin, P. G. J., Mason, J., Yang, J., & Dobinson, J. (2025). archNEMESIS: An Open-Source Python Package for Analysis of Planetary Atmospheric Spectra. *Journal of Open Research Software*, 13, 10. <https://doi.org/10.5334/jors.554>

Anguiano-Arteaga, A., Pérez-Hoyos, S., Sánchez-Lavega, A., Sanz-Querena, J. F., & Irwin, P. G. J. (2021). Vertical Distribution of Aerosols and Hazes Over Jupiter's Great Red Spot and Its Surroundings in 2016 From HST/WFC3 Imaging. *Journal of Geophysical Research: Planets*, 126(11). <https://doi.org/10.1029/2021JE006996>

Anguiano-Arteaga, A., Pérez-Hoyos, S., Sánchez-Lavega, A., Sanz-Querena, J. F., & Irwin, P. G. J. (2023). Temporal Variations in Vertical Cloud Structure of Jupiter's Great Red Spot, Its Surroundings and Oval BA From HST/WFC3 Imaging. *Journal of Geophysical Research: Planets*, 128(9). <https://doi.org/10.1029/2022JE007427>

Baines, K., Sromovsky, L.A., Fry, P.M., Carlson, R.W., & Momary, T.W. (2016). Accurate spectral fits of Jupiter's Great Red Spot: VIMS visual spectra modelled with chromophores created by photolyzed ammonia reacting with acetylene. *AAS/DPS Meeting 48*, id.508.08. <https://ui.adsabs.harvard.edu/abs/2016DPS....4850808B>

Baines, K.H., Sromovsky, L.A., Carlson, R.W., Momary, T.W., Fry, P.M. (2019). The visual spectrum of Jupiter's Great Red Spot accurately modelled with aerosols produced by photolyzed ammonia reacting with acetylene. *Icarus*, 330, 217–229. <https://doi.org/10.1016/j.icarus.2019.04.008>

Banfield, D., Gierasch, P.J., Bell, M., Ustinov, E., Ingersoll, A.P., Vasavada, A.R., West, R.A., & Belton, M.J.S. (1998). Jupiter's cloud structure from Galileo imaging data. *Icarus*, 135(1), 230–250. <https://doi.org/10.1006/icar.1998.5985>

Bar-Nun, A., Podolak, M. (1985). The contribution by thunderstorms to the abundances of CO, C<sub>2</sub>H<sub>2</sub>, and HCN on Jupiter. *Icarus*, 64(1), 112–124. [https://doi.org/10.1016/0019-1035\(85\)90042-9](https://doi.org/10.1016/0019-1035(85)90042-9)

Bétrémieux, Y., Yelle, R.V., & Griffith, C.A. (2003). HST observation of the atmospheric composition of Jupiter's equatorial region: Evidence for tropospheric C<sub>2</sub>H<sub>2</sub>. *Icarus*, 163, 414–427. [https://doi.org/10.1016/S0019-1035\(03\)00086-1](https://doi.org/10.1016/S0019-1035(03)00086-1)

Braude, A.S., Irwin, P.G.J., Orton, G.S., & Fletcher, L.N. (2020). Colour and tropospheric cloud structure of Jupiter from MUSE/VLT: Retrieving a universal chromophore. *Icarus*, 338, 113589. <https://doi.org/10.1016/j.icarus.2019.113589>

Cabane, M., Chassefière, E., Israel, G. (1992). Formation and growth of photochemical aerosols in Titan's atmosphere. *Icarus*, 96(2), 176–189. [https://doi.org/10.1016/0019-1035\(92\)90071-E](https://doi.org/10.1016/0019-1035(92)90071-E)

Carlson, R.W., Baines, K.H., Anderson, M.S., Filacchione, G., Simon, A.A. (2016). Chromophores from photolyzed ammonia reacting with acetylene: Application to Jupiter's Great Red Spot. *Icarus*, 274, 106–115. <https://doi.org/10.1016/j.icarus.2016.03.008>

Chatterjee, A., Kerker, M., Cooke, D. D. (1975). Brownian coagulation of aerosols in the transition regime. *Journal of Colloid and Interface Science*, 53(1), 71–82. [https://doi.org/10.1016/0021-9797\(75\)90036-3](https://doi.org/10.1016/0021-9797(75)90036-3)

Cheng, B.-M., Lu, H.-C., Chen, H.-K., Bahou, M., Lee, Y.-P., Mebel, A.M., Lee, L.C., Liang, M.-C., Yung, Y.L. (2006). Absorption cross sections of NH<sub>3</sub>, NH<sub>2</sub>D, NHD<sub>2</sub>, and ND<sub>3</sub> in the spectral range 140–220 nm and implications for planetary isotopic fractionation. *Astrophys. J.*, 647(2), 1535–1542. <https://doi.org/10.1086/505615>

Colaprete, A., Toon, O.B. (2003). Carbon dioxide clouds in an early dense Martian atmosphere. *J. Geophys. Res. Planets*, 108(E4), 5025. <https://doi.org/10.1029/2002JE001967>

Conrath, B. J., Flasar, F. M., Pirraglia, J. A., Gierasch, P. J., Hunt, G. E. (1981). Thermal structure and dynamics of the Jovian atmosphere. II. Visible cloud features. *Journal of Geophysical Research: Space Physics*, 86(A10), 8769–8775. <https://doi.org/10.1029/JA086iA10p08769>

Dahl, E.K., Chanover, N.J., Orton, G.S., Baines, K.H., Sinclair, J.A., Voelz, D.G., Wijerathna, E.A., Strycker, P.D., & Irwin, P.G.J. (2021). Vertical Structure and Color of Jovian Latitudinal Cloud Bands during the

Juno Era. *The Planetary Science Journal*, 2(1), 16. <https://doi.org/10.3847/PSJ/abd400>

Ferris, J.P., & Ishikawa, Y. (1987). HCN and chromophore formation on Jupiter. *Nature*, 326, 777–778. <https://doi.org/10.1038/326777a0>

Flasar, F. M., Conrath, B. J., Pirraglia, J. A., Clark, P. C., French, R. G., & Gierasch, P. J. (1981). Thermal Structure and Dynamics of the Jovian Atmosphere: 1. The Great Red Spot. *Journal of Geophysical Research: Space Physics*, 86(A10), 8759–8767. <https://doi.org/10.1029/JA086iA10p08759>

Fletcher, L.N., Orton, G.S., Greathouse, T.K., Rogers, J.H., Zhang, Z., Oyafuso, F.A., Eichstädt, G., Melin, H., Li, C., Levin, S.M., Bolton, S., Janssen, M., Mettig, H.J., Grassi, D., Mura, A., Adriani, A. (2020). Jupiter's Equatorial Plumes and Hot Spots: Spectral Mapping from Gemini/TEXES and Juno/MWR. *J. Geophys. Res. Planets*, 125(8), e06399. <https://doi.org/10.1029/2020JE006399>

Fletcher, L.N., Cavalie, T., Grassi, D., Hueso, R., Lara, L.M., Kaspi, Y., Galanti, E., Greathouse, T.K., Molyneux, P.M., Galand, M., Vallat, C., Witasse, O., Lorente, R., Hartogh, P., Poulet, F., Langevin, Y., Palumbo, P., Gladstone, G.R., Retherford, K.D., Dougherty, M.K., Wahlund, J.-E., Barabash, S., Iess, L., Bruzzone, L., & Costa, M. (2023). Jupiter Science Enabled by ESA's Jupiter Icy Moons Explorer. *Space Science Reviews*, 219, 53. <https://doi.org/10.1007/s11214-023-00988-8>

Friedlander, S. K. (2000). *Smoke, Dust, and Haze: Fundamentals of Aerosol Dynamics*. Oxford University Press, New York. Second edition.

Friedson, A. J. (1998). Formation of refractory grains in Shoemaker–Levy 9 fireballs. *Icarus*, 131(1), 179–197. <https://doi.org/10.1006/icar.1997.5853>

Friedson, A. J., Wong, A.-S., & Yung, Y. L. (2002). Models for polar haze formation in Jupiter's stratosphere. *Icarus*, 158(2), 389–400. <https://doi.org/10.1006/icar.2002.6885>

Fry, P., & Sromovsky, L. (2023). Investigating temporal changes in Jupiter's aerosol structure with rotationally-averaged 2015–2020 HST WFC3 images. *Icarus*, 389, 115224. <https://doi.org/10.1016/j.icarus.2022.115224>

Fuchs, N. A. (1964). *The Mechanics of Aerosols*. Pergamon Press. (Translated from Russian by E. Jachowicz, originally published in 1955 by the Academy of Sciences of the U.S.S.R.).

Gao, P., Marley, M.S., Zahnle, K., Robinson, T.D., Lewis, N.K. (2017). Sulfur hazes in giant exoplanet atmospheres: Impacts on reflected light spectra. *Astron. J.*, 153(3), 139. <https://doi.org/10.3847/1538-3881/aa5fab>

Gladstone, G.R., Allen, M., Yung, Y.L. (1996). Hydrocarbon Photochemistry in the Upper Atmosphere of Jupiter. *Icarus*, 119(1), 1–52. <https://doi.org/10.1006/icar.1996.0001>

Grassi, D., Mura, A., Sindoni, G., Adriani, A., Atreya, S.K., Filacchione, G., Fletcher, L.N., Lunine, J.I., Moriconi, M.L., Noschese, R., Orton, G.S., Plainaki, C., Sordini, R., Tosi, F., Turrini, D., Olivier, A., Eichstädt, G., Hansen, C.J., Melin, H., Altieri, F., Cicchetti, A., Dinelli, B.M., Migliorini, A., Piccioni, G., Stefani, S., & Bolton, S.J. (2021). On the clouds and ammonia in Jupiter's upper troposphere from Juno JIRAM reflectivity observations. *Monthly Notices of the Royal Astronomical Society*, 503, 4892–4907. <https://doi.org/10.1093/mnras/stab740>

Hansen, C.F. (1979). Viscosity and thermal conductivity of model Jupiter atmospheres. NASA Technical Memorandum 78556.

Hansen, J. E., & Travis, L. D. (1974). Light scattering in planetary atmospheres. *Space Science Reviews*, 16(4), 527–610. <https://doi.org/10.1007/BF00168069>

Harkett, J., Fletcher, L.N., King, O.R.T., Roman, M.T., Melin, H., Hammel, H.B., Hueso, R., Sánchez-Lavega, A., Wong, M.H., Milam, S.N., Orton, G.S., de Kleer, K., Irwin, P.G.J., de Pater, I., Fouchet, T., Rodríguez-Ovalle, P., Fry, P.M., & Showalter, M.R. (2024). The thermal structure and composition of Jupiter's Great Red Spot from JWST/MIRI. *JGR Planets*, 129, e2024JE008415. <https://doi.org/10.1029/2024JE008415>

Haynes, W. M. (Ed.). (2011). *CRC Handbook of Chemistry and Physics* (92nd ed.). CRC Press. ISBN: 978-1-4398-5511-9.

Hidy, G. M. & Brock, J. R. (2013). *The Dynamics of Aerocolloidal Systems: International Reviews in Aerosol Physics and Chemistry, Volume 1*. Elsevier.

Hue, V., Hersant, F., Cavalié, T., Dobrijevic, M., & Sinclair, J. A. (2018). Photochemistry, mixing and transport in Jupiter's stratosphere constrained by Cassini. *Icarus*, 307, 106–123. <https://doi.org/10.1016/j.icarus.2018.02.009>

Irwin, P. G. J., Teanby, N. A., de Kok, R., Fletcher, L. N., Howett, C. J. A., Tsang, C. C. C., Wilson, C. F., Calcutt, S. B., Nixon, C. A., & Parrish, P. D. (2008). The NEMESIS planetary atmosphere radiative transfer and retrieval tool. *Journal of Quantitative Spectroscopy and Radiative Transfer*, 109, 1136–1150. <https://doi.org/10.1016/j.jqsrt.2007.11.006>

Irwin, P.G.J. (2009). *Giant Planets of Our Solar System: Atmospheres, Composition, and Structure*. Springer Science & Business Media.

Irwin, P.G.J., Dobinson, J., James, A., Teanby, N.A., Simon, A.A., Fletcher, L.N., Roman, M.T., Orton, G.S., Wong, M.H., & Toledo, D. (2024). Modelling the seasonal cycle of Uranus's colour and magnitude, and comparison with Neptune. *Monthly Notices of the Royal Astronomical Society*, 527(4), 11521–11538. <https://doi.org/10.1093/mnras/stad3761>

Kasten, F. (1968). Falling Speed of Aerosol Particles. *Journal of Applied Meteorology*, 7(5), 944–946. [https://doi.org/10.1175/1520-0450\(1968\)007<0944:FSOAP>2.0.CO;2](https://doi.org/10.1175/1520-0450(1968)007<0944:FSOAP>2.0.CO;2)

de Kleer, K., Luszcz-Cook, S., de Pater, I., Ádámkovics, M., & Hammel, H. B. (2015). Clouds and aerosols on Uranus: Radiative transfer modeling of spatially-resolved near-infrared Keck spectra. *Icarus*, 256, 120–137. <https://doi.org/10.1016/j.icarus.2015.04.021>

Knížek, A., Rimmer, P.B., & Ferus, M. (2026). A full-atmosphere model of Jupiter. *Icarus*, 444, 116806. <https://doi.org/10.1016/j.icarus.2025.116806>

Loeffler, M.J., Hudson, R.L., Chanover, N.J., & Simon, A.A. (2016). The spectrum of Jupiter's Great Red Spot: The case for ammonium hydrosulfide (NH<sub>4</sub>SH). *Icarus*, 271, 265–268. <https://doi.org/10.1016/j.icarus.2016.02.010>

Marley, M.S., Ackerman, A.S., Cuzzi, J.N., Kitzmann, D. (2013). Clouds and hazes in exoplanet atmospheres. In: Mackwell, S.J., Simon-Miller,

A.A., Harder, J.W., Bullock, M.A. (Eds.), *Comparative Climatology of Terrestrial Planets*, Univ. of Arizona Press, Tucson, pp. 367–391.

McGouldrick, K., Toon, O.B. (2007). An investigation of possible causes of the holes in the condensational Venus cloud using a microphysical cloud model with a radiative-dynamical feedback. *Icarus*, 191(1), 1–24. <https://doi.org/10.1016/j.icarus.2007.04.007>

Mitchell, J. L., Beebe, R. F., Ingersoll, A. P., & Garneau, G. W. (1981). Flow fields within Jupiter's great red spot and white oval BC. *Journal of Geophysical Research: Space Physics*, 86(A10), 8751–8757. <https://doi.org/10.1029/JA086iA10p08751>

Moreno, F. (1996). The structure of the stratospheric aerosol layer in the equatorial and south polar regions of Jupiter. *Icarus*, 124(2), 632–644. <https://doi.org/10.1006/icar.1996.0237>

Moses, J.I., Fouchet, T., Bézard, B., Gladstone, G.R., Lellouch, E., Feuchtgruber, H. (2005). Photochemistry and diffusion in Jupiter's stratosphere: Constraints from ISO observations and comparisons with other giant planets. *J. Geophys. Res. Planets*, 110(E8), E08001. <https://doi.org/10.1029/2005JE002411>

Moses, J.I., Visscher, C., Keane, T.C., Sperier, A. (2010). On the abundance of non-cometary HCN on Jupiter. *Faraday Discuss.*, 147, 103–136. <https://doi.org/10.1039/c003954c>

Ordóñez-Etxeberria, I., Hueso, R., Sánchez-Lavega, A., & Pérez-Hoyos, S. (2016). Spatial distribution of jovian clouds, hazes and colors from Cassini ISS multi-spectral images. *Icarus*, 267, 34–50. <https://doi.org/10.1016/j.icarus.2015.12.008>

Pérez-Hoyos, S., Sanz-Requena, J. F., Barrado-Izagirre, N., Rojas, J. F., Sánchez-Lavega, A., & IOPW Team (2012a). The 2009–2010 fade of Jupiter's South Equatorial Belt: Vertical cloud structure models and zonal winds from visible imaging. *Icarus*, 217, 256–271. <https://doi.org/10.1016/j.icarus.2011.11.008>

Pérez-Hoyos, S., Sánchez-Lavega, A., Sanz-Requena, J.F., Barrado-Izagirre, N., Carrión-González, Ó., Anguiano-Arteaga, A., Irwin, P.G.J., & Braude,

A.S. (2020). Color and aerosol changes in Jupiter after a North Temperate Belt disturbance. *Icarus*, 352, 114031. <https://doi.org/10.1016/j.icarus.2020.114031>

Podolak, M., Bar-Nun, A. (1988). Moist convection and the abundances of lightning-produced CO, C<sub>2</sub>H<sub>2</sub>, and HCN on Jupiter. *Icarus*, 75(3), 566–570. [https://doi.org/10.1016/0019-1035\(88\)90165-0](https://doi.org/10.1016/0019-1035(88)90165-0)

Pollack, J.B., Rages, K., Pope, S.K., Tomasko, M.G., Romani, P.N., Atreya, S.K. (1987). Nature of the stratospheric haze on Uranus: Evidence for condensed hydrocarbons. *J. Geophys. Res.*, 92(A13), 15037–15065. <https://doi.org/10.1029/JA092iA13p15037>

Press, W. H., Teukolsky, S. A., Vetterling, W. T., & Flannery, B. P. (1992). *Numerical Recipes in Fortran 77: The Art of Scientific Computing* (2nd ed.). Cambridge University Press.

Pruppacher, H. R., Klett, J. D. (2010). *Microphysics of Clouds and Precipitation*. Springer Science & Business Media. Reprint of 1980 edition.

Roy-Perez, J., Pérez-Hoyos, S., Barrado-Izaguirre, N., & Chen-Chen, H. (2025). The role of cloud particle properties in the WASP-39b transmission spectrum based on JWST/NIRSpec observations. *Astronomy & Astrophysics*, 694, A249. <https://doi.org/10.1051/0004-6361/202450142>

Sánchez-Lavega, A. (2011). *An Introduction to Planetary Atmospheres*. CRC Press / Taylor & Francis.

Sánchez-Lavega, A., Legarreta, J., García-Melendo, E., Hueso, R., Pérez-Hoyos, S., Gómez-Forrellad, J. M., Fletcher, L. N., Orton, G. S., Simon-Miller, A., Chanover, N., Irwin, P., Tanga, P., & Cecconi, M. (2013). Colors of Jupiter's large anticyclones and the interaction of a Tropical Red Oval with the Great Red Spot in 2008. *Journal of Geophysical Research: Planets*, 118(12), 2537–2557. <https://doi.org/10.1002/2013JE004371>

Sánchez-Lavega, A., García-Melendo, E., Legarreta, J., Miró, A., Soria, M., & Ahrens-Velásquez, K. (2024). The origin of Jupiter's Great Red Spot. *Geophysical Research Letters*, 51, e2024GL108993. <https://doi.org/10.1029/2024GL108993>

Sitarski, M., Seinfeld, J. H. (1977). Brownian coagulation in the transition regime. *Journal of Colloid and Interface Science*, 61(2), 261–271. [https://doi.org/10.1016/0021-9797\(77\)90389-7](https://doi.org/10.1016/0021-9797(77)90389-7)

Sromovsky, L.A., Baines, K.H., Fry, P.M., Carlson, R.W. (2017). A possibly universal red chromophore for modeling color variations on Jupiter. *Icarus*, 291, 232–244. <https://doi.org/10.1016/j.icarus.2016.12.014>

Toledo, D., Irwin, P.G.J., Rannou, P., Teanby, N.A., Simon, A.A., Wong, M.H., Orton, G.S. (2019). Constraints on Uranus's haze structure, formation and transport. *Icarus*, 333, 1–11. <https://doi.org/10.1016/j.icarus.2019.05.018>

Toledo, D., Irwin, P.G.J., Rannou, P., Fletcher, L.N., Teanby, N.A., Wong, M.H., Orton, G.S. (2020). Constraints on Neptune's haze structure and formation from VLT observations in the H-band. *Icarus*, 350, 113808. <https://doi.org/10.1016/j.icarus.2020.113808>

Toon, O.B., Turco, R.P., Hamill, P., Kiang, C.S., Whitten, R.C. (1979). A one-dimensional model describing aerosol formation and evolution in the stratosphere: II. Sensitivity studies and comparison with observations. *J. Atmos. Sci.*, 36(4), 718–736. [https://doi.org/10.1175/1520-0469\(1979\)036<0718:AODMDA>2.0.CO;2](https://doi.org/10.1175/1520-0469(1979)036<0718:AODMDA>2.0.CO;2)

Toon, O.B., Turco, R.P., Pollack, J.B. (1980). A physical model of Titan's cloud. *Icarus*, 43, 260–282. [https://doi.org/10.1016/0019-1035\(80\)90173-6](https://doi.org/10.1016/0019-1035(80)90173-6)

Toon, O.B., Turco, R.P., Westphal, D., Malone, R., Liu, M.S. (1988). A Multidimensional Model for Aerosols – Description of Computational Analogs. *J. Atmos. Sci.*, 45, 2123–2143. [https://doi.org/10.1175/1520-0469\(1988\)045<2123:AMMFAD>2.0.CO;2](https://doi.org/10.1175/1520-0469(1988)045<2123:AMMFAD>2.0.CO;2)

Turco, R.P., Hamill, P., Toon, O.B., Whitten, R.C., Kiang, C.S. (1979a). A one-dimensional model describing aerosol formation and evolution in the stratosphere: I. Physical processes and mathematical analogs. *J. Atmos. Sci.*, 36(4), 699–717. [https://doi.org/10.1175/1520-0469\(1979\)036<0699:AODMDA>2.0.CO;2](https://doi.org/10.1175/1520-0469(1979)036<0699:AODMDA>2.0.CO;2)

Turco, R.P., Hamill, P., Toon, O.B., Whitten, R.C., & Kiang, C.S. (1979b). The NASA-Ames Research Center Stratospheric Aerosol Model. I. Physical Processes and Computational Analogs. NASA Technical Paper 1362.

West, R. A., Strobel, D. F., & Tomasko, M. G. (1986). Clouds, aerosols, and photochemistry in the Jovian atmosphere. *Icarus*, 65(2–3), 161–217.  
[https://doi.org/10.1016/0019-1035\(86\)90135-1](https://doi.org/10.1016/0019-1035(86)90135-1)

West, R.A., Baines, K.H., Friedson, A.J., Banfield, D., Ragent, B., & Taylor, F.W. (2004). Jovian clouds and haze. In Bagenal, F., Dowling, T.E., & McKinnon, W.B. (Eds.), *Jupiter: The Planet, Satellites and Magnetosphere* (pp. 79–104). Cambridge University Press.